Journal of Fluorine Chemistry 219 (2019) 10–22

Contents lists available at ScienceDirect

Journal of Fluorine Chemistry

journal homepage: www.elsevier.com/locate/fluor

Influence of 2′-fluoro modification on glycosidic bond stabilities and gas-phase ion structures of protonated pyrimidine nucleosides

Zachary J. Devereaux[a], H.A. Roy[a], C.C. He[a], Y. Zhu[a], N.A. Cunningham[a], L.A. Hamlow[a], G. Berden[b], J. Oomens[b], M.T. Rodgers[a,*]

[a] Wayne State University, Department of Chemistry, 5101 Cass Avenue, Detroit, MI 48202, United States
[b] Radboud University, Institute for Molecules and Materials, FELIX Laboratory, Toernooiveld 7c, 6525 ED Nijmegen, The Netherlands

ARTICLE INFO

Keywords:
Modified pyrimidine nucleosides
Energy-resolved collision-induced dissociation (ER-CID)
Survival yield analysis
Infrared multiple photon dissociation (IRMPD) action spectroscopy
Fluorine hydrogen-bond
Free electron laser

ABSTRACT

The effects of 2′-fluoro substitution on the protonated gas-phase ions of the pyrimidine nucleosides are examined and compared with their previously reported canonical RNA and DNA forms. *N*-Glycosidic bond cleavage is the only collision-induced dissociation (CID) fragmentation pathway of protonated 2′-fluoro-2′-deoxycytidine, $[Cydfl+H]^+$, and the major pathway of protonated 2′-fluoro-2′-deoxyuridine, $[Urdfl+H]^+$. Based on energy-resolved CID and survival yield analysis, the *N*-glycosidic bond of $[Cydfl+H]^+$ is more stable than that of $[Urdfl+H]^+$. Further, the *N*-glycosidic bond stability of protonated pyrimidine nucleosides increases with increasing 2′-substituent electronegativity and follows the order F > OH > H. Gas-phase conformations of $[Cydfl+H]^+$ and $[Urdfl+H]^+$ are studied via infrared multiple photon dissociation (IRMPD) action spectroscopy coupled with theoretical calculations. IRMPD action spectra are measured over the IR fingerprint and hydrogen-stretching regions. Comparisons of theoretical and experimental spectra indicate that the experimentally accessed $[Cydfl+H]^+$ and $[Urdfl+H]^+$ conformers are highly parallel to those populated for their canonical counterparts. Evidence for gas-phase intramolecular O3′H···F2′ hydrogen-bonding in the IRMPD spectra of $[Cydfl+H]^+$ and $[Urdfl+H]^+$ allows for more definitive sugar puckering determinations than possible in the analogous canonical nucleosides.

1. Introduction

Nucleosides are the building blocks of the genetic biopolymers, deoxyribonucleic acid (DNA) and ribonucleic acid (RNA). The canonical nucleoside constituents of DNA and RNA differ only in the functionality of the 2′-substituent of their sugar moieties; in DNA this 2′-substituent is a hydrogen atom, whereas in RNA it is a hydroxyl group. This singular functional group change fundamentally gives rise to the principal differences in macromolecular structure and biochemical activity between DNA and RNA [1].

Fluorine, the most electronegative element in the periodic table [2], can impart considerable effects on physicochemical and electronic properties of molecules including bond strengths, polarizabilities, dipole moments, acidity or basicity of proximal functional groups, and lipophilicity [3–5]. Pauling electronegativities of fluorine and oxygen are similar at 3.98 and 3.44, respectfully, and much larger than that of hydrogen at 2.20 [2]. The highly electronegative nature of fluorine results in covalent C–F bonds having significant ionic/electrostatic character and thus substantial dipole moments that interact indirectly with the nearby inter- and intramolecular chemical environment [4,5]. Fluorine is also quite small with a size intermediate between that of hydrogen and oxygen [5,6]: tertiary alkyl fluorine has a van der Waals radius of 1.47 Å, a hydroxyl group oxygen has a radius of 1.52 Å, and a hydrogen atom has a radius of 1.20 Å [7]. While hydroxyl groups may serve as hydrogen-bond donors and acceptors, fluorine is somewhat controversially recognized as a hydrogen-bond acceptor, as the lower polarizability of fluorine compared with oxygen weakens its electrostatic effects and causes it to form hydrogen-bond interactions that are often difficult to discern in the condensed phase [6,8–14]. However, due to its hydrogen-bonding and electrostatic interaction capabilities, as well as size similarity with hydrogen and hydroxyl groups, fluorine has commonly found use as an enzyme substrate analogue that imposes only minor steric demands on the enzyme [15].

Modern medicinal chemistry employs the unique properties of fluorine extensively [3,15–25]. In 2010 it was calculated that ~20% of prescribed drugs contained fluorine [26]. Additionally, the pyrimidine nucleoside analogues, with cytosine (Cyt) and uracil (Ura) nucleobases, have found particular applicability in pharmaceuticals as many display

* Corresponding author.
E-mail address: mrodgers@chem.wayne.edu (M.T. Rodgers).

https://doi.org/10.1016/j.jfluchem.2018.12.004
Received 10 September 2018; Received in revised form 6 December 2018; Accepted 9 December 2018
Available online 11 December 2018
0022-1139/

anti-cancer and anti-viral characteristics [27]. For example, gemcitabine, a cytidine derivative that is difluorinated at the C2′ position of the sugar, is an anti-cancer prodrug used to inhibit DNA synthesis and cause apoptosis of rapidly replicating cancer cells [28]. 5-Fluorouracil and 5-fluoro-2′-deoxyuridine, also known as floxuridine, have now been used in cancer treatments for over 50 years [29,30]. 2′-Deoxy-5-fluoro-3′-thiacytidine, or emtricitabine, has found widespread use as an anti-viral medication in the treatment of human immunodeficiency virus (HIV) [31]. As a statement to their societal value, gemcitabine, 5-fluorouracil, and emtricitabine are on the World Health Organization's Model List of Essential Medicines [32].

A fundamental understanding of the intrinsic properties of natural and synthetic genetic material constituents is desired due to their vast importance and effects in biological systems. Many studies have elucidated the intrinsic gas-phase ion structural and energetic properties of protonated and metal cationized nucleobases [33–37], nucleosides [35,38–47], and nucleotides [48–52]. Systematic studies of modified nucleosides compared with their canonical counterparts may provide a fundamental understanding useful in extracting trends relevant to biochemical activity and drug design. In this work, the relative glycosidic bond stabilities and gas-phase ion structures of the protonated pyrimidine 2′-fluoro-2′-deoxynucleosides (Nuofl), 2′-fluoro-2′-deoxycytidine (Cydfl) and 2′-fluoro-2′-deoxyuridine (Urdfl), are studied using tandem mass spectrometry (MS/MS) approaches and electronic structure calculations. Unimolecular dissociation mass spectra and relative glycosidic bond stabilities are determined via energy-resolved collision-induced dissociation (ER-CID) and survival yield analyses of the ER-CID data. Experimentally populated gas-phase $[Cydfl+H]^+$ and $[Urdfl+H]^+$ ion structures are determined via spectral comparisons of experimental infrared multiple photon dissociation (IRMPD) action spectra with theoretical linear IR spectra predicted from density functional theory calculations. ER-CID and IRMPD behaviors are compared. Results for $[Nuofl+H]^+$ are compared with results for their canonical counterpart 2′-deoxyribonucleosides (dNuo) and ribonucleosides (Nuo) [40,41,43,44] to elucidate the effects of 2′-fluoro substitution on their dissociation behaviors, relative energetic stabilities, and three-dimensional gas-phase structures.

2. Experimental and computational methods

2.1. Materials and locations

Cydfl and Urdfl were purchased from Hongene Biotechnology Limited (Morrisville, NC) and used as supplied. Neutral structures and atom numbering schemes for Cydfl, Urdfl, and their counterpart dNuo and Nuo nucleosides are shown in Fig. 1. ER-CID experiments were performed at Wayne State University (WSU; Detroit, MI, United States). For these experiments, methanol (HPLC grade) and glacial acetic acid were purchased from Fisher Scientific (Waltham, MA, United States) and water (HPLC grade) was purchased from Sigma-Aldrich Corporation (St. Louis, MO, United States). IRMPD action spectroscopy experiments were performed at the FELIX Laboratory at Radboud University (Nijmegen, The Netherlands). For these experiments, methanol (HPLC grade), water (HPLC grade), and fuming hydrochloric acid were purchased from Sigma-Aldrich Corporation (St. Gallen, Switzerland).

2.2. Mass spectrometry and energy-resolved collision-induced dissociation

ER-CID experiments were performed in triplicate on a Bruker amaZon ETD quadrupole ion trap mass spectrometer (QIT MS; Billerica, MA, United States). Separate 10 μm solutions of Cydfl and Urdfl were prepared in 50%/50% methanol/water (v/v) + 1% acetic acid. $[Cydfl+H]^+$ and $[Urdfl+H]^+$ were formed by direct infusion of the acidified nucleoside solution to an Apollo II electrospray ionization (ESI) source at ~3 μL/min and transferred through the instrument into the QIT where ER-CID was performed on the relevant mass-isolated protonated nucleoside. Helium present in the QIT aided ion trapping through collisional cooling and was also used as the collision gas. The QIT radio-frequency (rf) excitation amplitude was varied in 0.01 V steps from 0.00 V to a voltage that exceeds the excitation amplitude where the precursor ion signal intensity was completely depleted. The total mass spectra collection time per rf excitation voltage step was 30 s. The CID fragmentation excitation time within each analysis sequence was set to 40 ms. With the mass analysis sequence parameters used, 48 mass spectra were averaged at each rf excitation voltage. Compass Data Analysis 4.0 (Bruker Daltonics, Bremen, Germany) was used to acquire, extract, and export the mass spectral data.

2.3. Survival yield analysis of ER-CID data

Survival yield analysis, when properly employed, is a reliable method for determining relative precursor ion stability [39,41,42,44,53–57]. ER-CID experiments and survival yield analyses were performed and reported previously for the protonated forms of cytidine (Cyd), 2′deoxycytidine (dCyd) [41], uridine (Urd), and 2′-deoxyuridine (dUrd) [44]. Data taken from these references is compared with results for $[Cydfl+H]^+$ and $[Urdfl+H]^+$ determined here. Care was taken to employ parallel experimental procedures and instrument parameters as necessary to provide directly comparable results. The precursor ion survival yields were calculated at each rf excitation energy per Eq. (1) [55]:

$$\text{Survival Yield} = I_p \,/\, (I_p + \sum I_f) \quad (1)$$

where I_p is the precursor ion intensity and ΣI_f is the sum of all fragment ion intensities. Survival yields were plotted as a function of rf excitation amplitude for each system. The data was fit with a four-parameter logistic dynamic curve [39,41,42,44], and the rf excitation amplitude required for 50% dissociation of the precursor ion ($CID_{50\%}$) was determined from the fit. Trends in the $CID_{50\%}$ values for the various systems are examined to elucidate their relative stabilities. SigmaPlot Version 10.0 (Systat Software, Inc., San Jose, CA, United States) was used to fit, analyze, and plot the data. Survival yields were calculated from mass spectral data extracted by Bruker software using custom software developed in our laboratory.

2.4. Mass spectrometry and IRMPD action spectroscopy

Cydfl and Urdfl were shipped from WSU to the FELIX Facility (Radboud University Nijmegen, The Netherlands) where ~1 mM solutions were prepared in 50%/50% methanol/water (v/v) + 1% hydrochloric acid. IRMPD action spectra were acquired in a parallel fashion to previous experiments [38–44,47] using a homebuilt 4.7 T Fourier transform ion cyclotron resonance mass spectrometer (FT-ICR MS) coupled with two sources of tunable IR laser light: the free electron laser for infrared experiments (FELIX) [58] for measurements in the IR fingerprint region (~600–1850 cm^{-1}), and a benchtop optical parametric oscillator/optical parametric amplifier (OPO) laser system (LaserVision, Bellevue, WA, United States) pumped by an InnoLas SpitLight 600 Nd:YAG (Krailling, Germany) for measurements in the hydrogen-stretching region (~3300–3800 cm^{-1}). Protonated Cydfl and Urdfl were formed by spraying in a Micromass "Z-Spray" ESI source (Now part of the Waters Corporation; Milford, MA, United States) at ~5 μL/min, accumulated in an rf hexapole ion trap for several seconds to increase ion signal and allow thermalization, then pulsed through a quadrupole bender and injected into the ICR cell where they were trapped, mass isolated by stored waveform inverse Fourier transform (SWIFT) [59] and irradiated with an IR laser to induce photodissociation. When the trapped ions possess a vibrational frequency resonant with the incident laser light, light is absorbed. The energy absorbed is redistributed among the molecular ion via intramolecular vibrational redistribution [60]. When enough energy is absorbed and redistributed

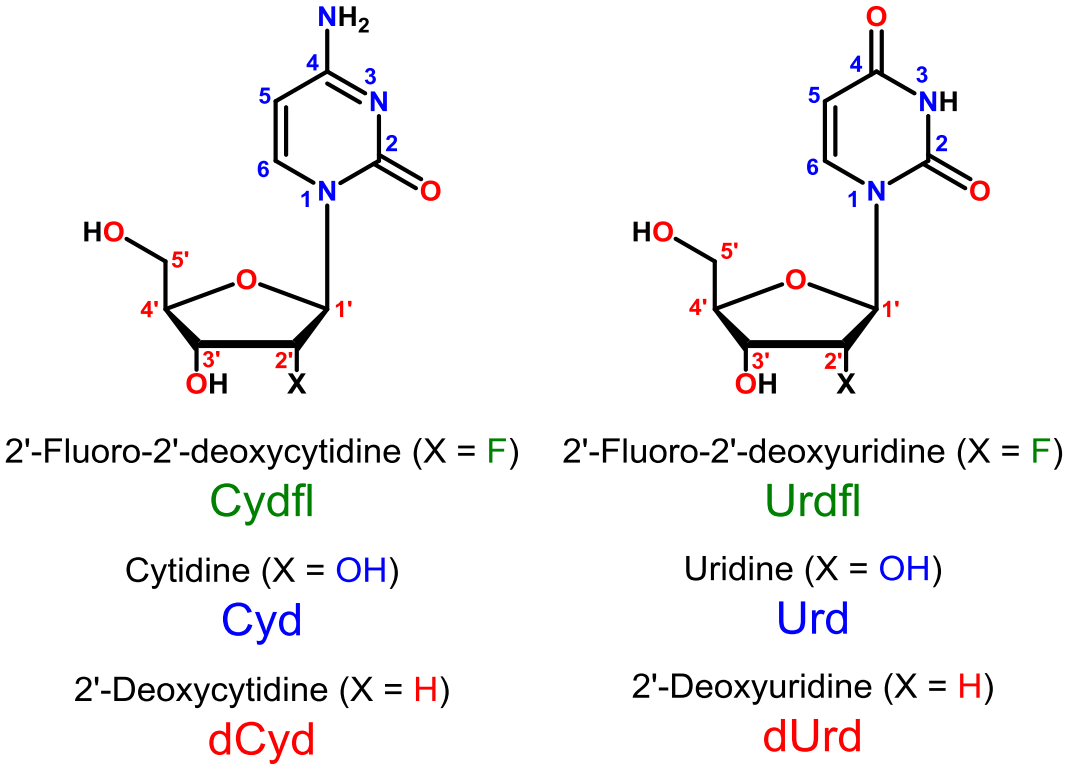

Fig. 1. Chemical structures of the neutral pyrimidine nucleosides compared in this work. 2′-Fluoro-2′-deoxycytidine (Cydfl) and 2′-fluoro-2′-deoxyuridine (Urdfl) have a 2′-F, cytidine (Cyd) and uridine (Urd) have a 2′-OH, and 2′-deoxycytidine (dCyd) and 2′-deoxyuridine (dUrd) have a 2′-H. The numbering of the atoms of the nucleobase and sugar moieties are shown.

throughout the internal energy modes of the ion, typically on the order of tens to hundreds of photons, unimolecular dissociation occurs. This dissociation is the "action" detected by the mass spectrometer as precursor ion intensity depletion and fragment ion intensity enhancement. Laser power and interaction time with the ion cloud were tuned to achieve sufficient fragmentation without signal saturation, i.e. generally > 50% of the precursor ion intensity remained during the experiments even for the most intense absorptions. For the previously examined protonated dCyd, Cyd, dUrd, and Urd ions the FELIX laser was operated at 10 Hz and the ions were irradiated for 2.5 to 3.6 s [40,43]; for the protonated Cydfl and Urdfl ions examined here, FELIX was operated at 5 Hz and the ions were irradiated for 3.0 and 3.5 s, respectively. No FELIX laser attenuation was used. For the OPO measurements, the previously examined protonated dCyd, Cyd, dUrd, and Urd ions were irradiated for 5 to 10 s with and without additional CO_2 laser energy pumping [40,43] to increase the on-resonance dissociation yield [61]. Similar irradiation times were used for $[Cydfl+H]^+$ and $[Urdfl+H]^+$, examined here, without the use or need for additional CO_2 laser irradiation. IRMPD yields were calculated as a function of laser wavelength for each system per Eq. (2):

$$\text{IRMPD Yield} = \sum I_f \,/\, (I_p + \sum I_f) \qquad (2)$$

where I_p and ΣI_f are defined as in Eq. (1). Calculated IRMPD yields were normalized linearly based on the length of irradiation time and a least-squares fit of the laser power as a function of wavelength. IRMPD spectra measured for $[Cydfl+H]^+$ and $[Urdfl+H]^+$ are compared with predicted linear IR spectra in Section 3.4. calculated as described in Section 2.5.

2.5. Computational details

Calculations for $[Cyd+H]^+$, $[dCyd+H]^+$, $[Urd+H]^+$, and $[dUrd+H]^+$ were performed and described previously by Wu et al. [40,43]. The low-energy structures determined for these systems were taken for comparison with $[Nuofl+H]^+$ calculations performed in a parallel fashion in this work. Refer to Fig. 1 for molecular structures and atom numbering of the neutral pyrimidine nucleosides. Favorable protonation sites for Cydfl and Urdfl were investigated. For $[Cydfl+H]^+$ this included protonation at N3, O2, and F. For $[Urdfl+H]^+$ protonation at O2, O4, and F, and the protonated 2,4-dihydroxy tautomer were examined. Candidate structures for each protonated form of Cydfl and Urdfl were generated via a simulated annealing procedure using HyperChem software [62] and the Amber 3 force field. The simulated annealing procedure comprised heating each nucleoside ion form from 0 to 1000 K over 0.3 ps, sampling of conformational space at 1000 K for 0.2 ps, and cooling back to 0 K over 0.3 ps. The resulting structure was then optimized to a local minimum, and a snapshot of this structure was saved and used to initiate the next simulated annealing cycle. This process was repeated 300 times, and the 30 lowest energy structures for each site of protonation for each nucleoside was subjected to density functional theory (DFT) calculations. Previously found conformers of $[Nuo+H]^+$ and $[dNuo+H]^+$ and chemical knowledge were used to build additional structures to complement those generated by the simulated annealing procedure in order to comprehensively sample possible low-energy conformations, with particular attention paid to ensure thorough sampling of the sites of protonation, nucleobase orientation, sugar puckering, and hydrogen-bonding interactions. The Gaussian 09 suite of programs [63] was used to perform geometry optimizations, frequency analyses, and single point energy determinations. Geometry optimizations and frequency analyses were performed at the B3LYP/6-311+G(d,p) level of theory at standard ambient temperature and pressure and with a frequency scaling factor of 0.9887 [64]. Theoretical linear IR line spectra were generated from the vibrational analyses and scaled by a factor of 0.980 in the fingerprint region for both ions and by 0.957 and 0.954 for $[Cydfl+H]^+$ and $[Urdfl+H]^+$ in the hydrogen-stretching region, respectively. Predicted linear IR spectra were broadened using 30 cm^{-1} and 15 cm^{-1} full-width-at-half-

maximum Gaussian line shape convolution for the fingerprint and hydrogen-stretching regions, respectively, to account for the room temperature distribution of the ions and the bandwidth of the lasers used. Single point energy calculations were performed at the B3LYP/6-311 + G(2d,2p) and MP2(full)/6-311 + G(2d,2p) levels of theory on the optimized structures, and zero-point energy (ZPE) and thermal corrections at 298 K were included using the vibrational frequencies calculated at the B3LYP/6-311 + G(d,p) level of theory. In order to more fully analyze preferential sugar puckerings, additional single point energy calculations at the B3LYP/6-311 + G(2d,2p) and MP2(full)/6-311 + G(2d,2p) levels of theory were performed on select experimentally-relevant conformers using the polarizable continuum model (PCM) with an implicit water solvent.

3. Results and discussion

3.1. ER-CID mass spectrometry and survival yield analyses

3.1.1. CID pathways in the QIT MS

In the QIT, auxiliary rf excitation applied in resonance with the ion secular frequency excites the trapped ions increasing their trajectory radius and kinetic energy [65]. Consequently, through multiple collisions of the excited ions with the neutral He bath gas, some of the ion kinetic energy is converted into internal energy inducing unimolecular dissociation once the internal energy exceeds the dissociation threshold. The slow, stepwise heating in this multiple-collision CID process generally results in the most labile bonds being broken.

Mass spectra at an rf excitation amplitude producing ~50% dissociation of $[Cydfl+H]^+$ and $[Urdfl+H]^+$ are shown in Fig. 2, along with their previously reported counterpart $[Nuo+H]^+$ and $[dNuo+H]^+$ ions [41,44]. The dominant $[Nuofl+H]^+$ CID dissociation channels involve cleavage of the glycosidic bond, abstraction of a proton by the nucleobase from the sugar, and release of the protonated Cyt or Ura nucleobase as described in reactions (3) and (4).

$$[Cydfl + H]^+ \xrightarrow{n\,He} [Cyt + H]^+ + (Cydfl\text{–}Cyt) \quad (3)$$

$$[Urdfl + H]^+ \xrightarrow{n\,He} [Ura + H]^+ + (Urdfl\text{–}Ura) \quad (4)$$

Glycosidic bond cleavage, reaction (3), was the only dissociation reaction observed for $[Cydfl+H]^+$, behavior parallel to that observed for the canonical analogues $[Cyd+H]^+$ and $[dCyd+H]^+$ [41]. The dominant CID fragmentation pathway for $[Urdfl+H]^+$ also involves glycosidic bond cleavage, reaction (4), but in this case neutral losses of 42 Da and 60 Da were also observed. Neutral sequential losses of ketene (K; C_2H_2O) and water (W) were proposed as the neutral loss products as described in reactions (5) and (6).

$$[Urdfl + H]^+ \xrightarrow{n\,He} [Urdfl\text{–}K + H]^+ + K \quad (5)$$

$$[Urdfl\text{–}K + H]^+ \xrightarrow{n\,He} [Urdfl\text{–}K\text{–}W + H]^+ + K + W \quad (6)$$

$[Urd+H]^+$ displayed parallel fragmentation to $[Urdfl+H]^+$, but with an additional very minor $[Urd–W+H]^+$ product ion. $[dUrd+H]^+$ showed much richer CID fragmentation behavior where glycosidic bond cleavage producing $[Ura+H]^+$ was not the major pathway [44]. Instead, sequential water loss without glycosidic bond cleavage producing $[dUrd–W+H]^+$ and $[dUrd–2W+H]^+$ was observed as the major fragment ions. Additional minor dissociation channels arising from glycosidic bond cleavage, as well as glycosidic bond cleavage and water loss, generating product ions including $[Ura+H]^+$, $[dUrd–Ura+H]^+$, $[dUrd–Ura–W+H]^+$, and $[dUrd–Ura–2W+H]^+$. The similar CID fragmentation behavior of $[Urdfl+H]^+$ and $[Urd+H]^+$ suggests that 2′-fluoro and 2′-hydroxy substitution of the DNA nucleoside results in similar chemical consequences.

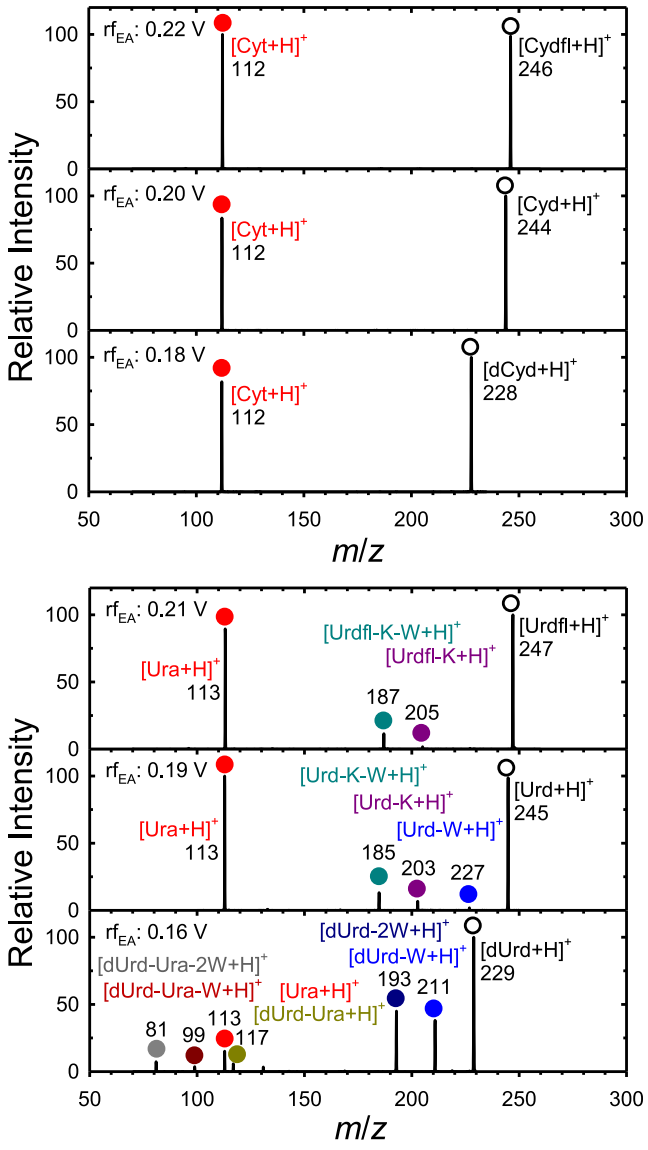

Fig. 2. CID mass spectra acquired at an rf excitation amplitude (rf_{EA}) that produced ~50% dissociation of $[Cydfl+H]^+$, $[Cyd+H]^+$, and $[dCyd+H]^+$ (top); $[Urdfl+H]^+$, $[Urd+H]^+$, and $[dUrd+H]^+$ (bottom). Results for the protonated canonical RNA and DNA nucleosides are reproduced from previous work [41,44].

3.1.2. Survival yields and relative glycosidic bond stabilities

Survival yield curves for $[Cydfl+H]^+$ and $[Urdfl+H]^+$ are compared with analogous data taken from prior work on $[Cyd+H]^+$, $[dCyd+H]^+$, $[Urd+H]^+$, and $[dUrd+H]^+$ [41,44] in Fig. 3. The survival yield curves adopt a characteristic "S"-shaped or sigmoidal curve, where initially at low excitation voltages no fragmentation occurs and consequently produce a maximum survival yield, as the critical energy threshold is reached and surpassed an increasing part of the ion population fragments and a concomitant decrease in survival yield is observed until complete precursor ion dissociation is achieved, and a minimum survival yield is reached.

Because all ion dissociation pathways proceed in a primarily parallel fashion dominated by cleavage of the N1–C1′ glycosidic bond, the survival yield $CID_{50\%}$ values can be used to provide a relative measure of the glycosidic bond stability of the protonated nucleosides. The $CID_{50\%}$ values, and therefore the glycosidic bond stability of the

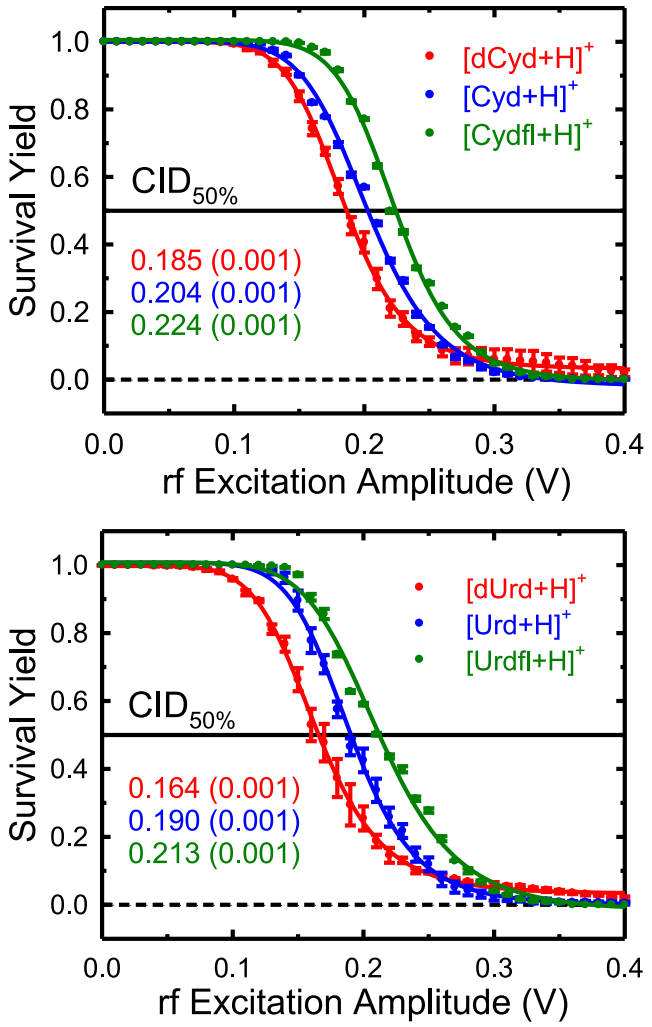

Fig. 3. Survival yield curves for $[Cydfl+H]^+$, $[Cyd+H]^+$, and $[dCyd+H]^+$ (top); $[Urdfl+H]^+$, $[Urd+H]^+$, and $[dUrd+H]^+$ (bottom). Error bars represent one standard deviation of the data measured in triplicate. Fits to the survival yield measurements using a dynamic four-parameter logistic curve, the extracted $CID_{50\%}$ values (and the standard error associated with the fit) are shown. Survival yield curves for the protonated canonical RNA and DNA nucleosides are taken from previous work [41,44].

protonated Cyd nucleosides exceeds that of the protonated Urd nucleosides (see Fig. 3). The second trend observed in Fig. 3 relates glycosidic bond strength to the 2′-substituent of the nucleosides, where glycosidic bond strengths increase in the order 2′-H < 2′-OH < 2′-F. The observed glycosidic bond strength trend can be understood based on the electronegativities of the 2′-substituents relative to the C2′ carbon: hydrogen is a weakly electropositive atom compared to carbon, whereas hydroxyl is highly electronegative due to its oxygen atom, and fluorine is the most electronegative of all atoms. The high electronegativity of the 2′-fluoro (and 2′-hydroxyl) substituent withdraws electron density from the C2′ atom giving it partial electropositivity, destabilizing the oxocarbenium ion intermediate, and thereby deactivating the glycosidic bond and making it less accessible for chemical reaction.

The *N*-glycosidic bond is especially relevant to the base-excision repair mechanism as increased bond strength can lower the rate of the enzymatic hydrolysis and base excision reaction and can therefore slow or stop the repair mechanism [66]. Increased glycosidic bond strength provided by 2′fluoro substituents can potentially increase anti-cancer properties by preventing the base-excision repair process, ultimately leading to apoptosis of the cells with stalled replication [67].

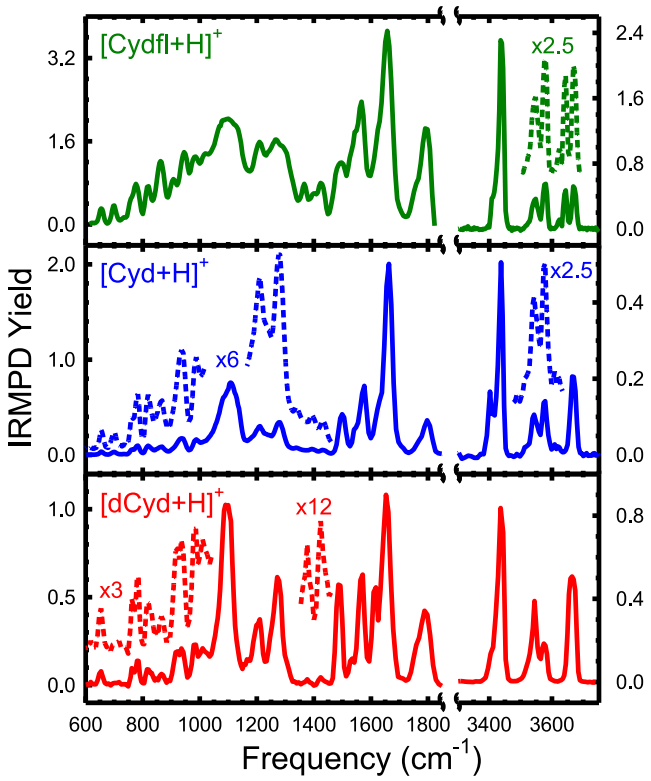

Fig. 4. Experimental IRMPD action spectra of $[Cydfl+H]^+$, $[Cyd+H]^+$, and $[dCyd+H]^+$. Data for the protonated canonical DNA and RNA nucleosides taken from previous work [40].

3.2. IRMPD action spectroscopy

IRMPD action spectroscopy [68] experiments for $[Cydfl+H]^+$ and $[Urdfl+H]^+$ were performed and reported here for the first time, whereas IRMPD action spectroscopy experiments for $[Cyd+H]^+$, $[dCyd+H]^+$, $[Urd+H]^+$, and $[dUrd+H]^+$ were performed and reported previously by Wu et al. [40,43] and the spectra are used here for comparisons. Fig. 4 compares the IRMPD action spectra of $[Cydfl+H]^+$ to those of $[Cyd+H]^+$ and $[dCyd+H]^+$. Fig. 5 compares the IRMPD action spectra of $[Urdfl+H]^+$ to those of $[Urd+H]^+$ and $[dUrd+H]^+$. IRMPD action spectra of gas-phase ions are generally parallel with condensed-phase linear IR absorption spectra. The fingerprint region, from ~600–1850 cm^{-1}, contains complex combinations of numerous C–C, C–N, and C–O single and double bond stretches, as well as carbon-backbone and hydrogen-bending modes. The hydrogen-stretching region, from ~3300–3800 cm^{-1}, exhibits N–H and O–H stretches and in-plane bends, which are sharp and relatively well-defined due to the lack of intermolecular hydrogen-bonding and solvation interactions in the gas-phase.

3.2.1. Photodissociation pathways in the FT-ICR MS

Photodissociation of $[Cydfl+H]^+$ and $[Urdfl+H]^+$ occurred exclusively through glycosidic bond cleavage producing $[Cyt+H]^+$ and $[Ura+H]^+$ as shown in reactions (7) and (8), respectively.

$$[Cydfl + H]^+ \xrightarrow{n\,h\nu} [Cyt + H]^+ + (Cydfl\text{–}Cyt) \quad (7)$$

$$[Urdfl + H]^+ \xrightarrow{n\,h\nu} [Ura + H]^+ + (Urdfl\text{–}Ura) \quad (8)$$

$[Urdfl+H]^+$ therefore displayed slight dissimilarities between the CID and IRMPD fragmentation as $[Urdfl–K+H]^+$ and $[Urdfl–K–W+H]^+$ were observed upon CID, but not for IRMPD. Both CID and IRMPD are slow step-wise ion heating methods where energy is slowly transferred into the internal modes of the system through absorption of

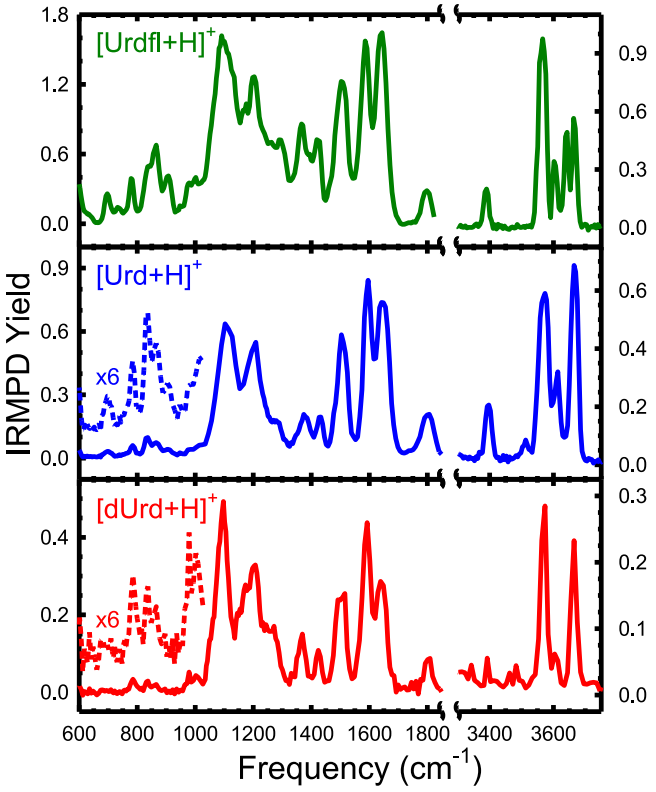

Fig. 5. Experimental IRMPD action spectra of $[Urdfl+H]^+$, $[Urd+H]^+$, and $[dUrd+H]^+$. Data for the protonated canonical DNA and RNA nucleosides taken from previous work [43].

multiple IR photons or multiple ion-neutral collisions such that both processes often produce fragmentation involving the lowest energy pathways. For that reason it might be expected that the fragmentation pathways observed would be highly parallel, as found for $[Cydfl+H]^+$. However, the additional CID product ions observed for $[Urdfl+H]^+$ suggest that heating via multiple collisions with He is slightly more rapid than multiple IR photon absorption, allowing for more energy to be pumped into the system prior to dissociation and thus accessing additional low-energy fragmentation channels. Similar disparities between CID and IRMPD were also recently observed in the dissociation of the [Ura + Cu]$^+$ complex [37].

3.2.2. IRMPD yield comparisons

It is difficult to make absolute conclusions based on normalized IRMPD yield intensities due to effects from, for example, changes in laser overlap with the ion cloud and anharmonicities of the vibrational modes, especially when experiments are performed across multiple days as is the case here. However, the general trends in intensity are often reliable with similar experiments through time and thus are briefly examined. Figure S1 overlays the $[Cydfl+H]^+$, $[Cyd+H]^+$, and $[dCyd+H]^+$ IRMPD spectra and $[Urdfl+H]^+$, $[Urd+H]^+$, and $[dUrd+H]^+$ IRMPD spectra so as to provide a visual comparison of their relative IRMPD yields. As reported previously, $[Cyd+H]^+$ and $[Urd+H]^+$ generally exhibit higher IRMPD yields than $[dCyd+H]^+$ and $[dUrd+H]^+$ in the fingerprint region. In contrast, the IRMPD yield for $[dCyd+H]^+$ in the hydrogen-stretching region exceeds that of $[Cyd+H]^+$, whereas the IRMPD yield of $[dUrd+H]^+$ is lower than $[Urd+H]^+$ [40,43]. Increased IRMPD yields in the hydrogen-stretching region were rationalized as originating from the increased numbers of free hydrogen stretches, either due to more bound hydrogen stretches as in $[dCyd+H]^+$ or by increased tautomerization as in $[Urd+H]^+$. When measuring the fingerprint IRMPD spectra, the FELIX laser was operated at 5 Hz for $[Nuofl+H]^+$ and at 10 Hz for $[dNuo+H]^+$ and $[Nuo+H]^+$, with similar irradiation times used in all systems. Due to the halved laser shot frequency, the IRMPD yields of $[Cydfl+H]^+$ and $[Urdfl+H]^+$ are effectively double that which are shown in Figure S1, but are scaled down by a factor of two to facilitate comparisons with $[Nuo+H]^+$ and $[dNuo+H]^+$. In the hydrogen-stretching region, the $[dNuo+H]^+$ and $[Nuo+H]^+$ ions used additional energy-level pumping with a CO_2 laser in order to achieve the desired fragmentation efficiency, whereas the $[Nuofl+H]^+$ ions did not require such augmentation of the OPO output. Thus, it can be concluded that the $[Nuofl+H]^+$ ions exhibit greater absorptivity than $[Nuo+H]^+$ and $[dNuo+H]^+$ ions at nearly all wavelengths.

Based solely on the IRMPD yields, it appears that the $[Nuofl+H]^+$ ions have the lowest glycosidic bond strengths, as they produce the highest yields and therefore a higher percentage of precursor ions undergo gas-phase unimolecular glycosidic bond cleavage. However, the survival yield results described in Section 3.1.2. clearly indicate that the 2′-fluoro modified nucleosides have the highest N1–C1′ glycosidic bond strengths among these systems. This apparent contradiction necessitates other factors for rationalization. One explanation is that the three lone electron pairs on the 2′-fluoro substituent provide higher IR absorption cross sections over the entire frequency range than the two lone pairs of the 2′-hydroxyl substituent and the lack of lone pairs on the 2′-hydrogen. It is also hypothesized that the high electronegativity of the 2′-fluoro substituent increases the dipole moments of at least some stretching and bending vibrations in the molecular ion, and therefore these modes display larger cross sections for IR absorption. A comparison of the electrostatic potential maps of the ground conformers of each majorly populated protonation site and the geometry optimized neutral calculated when simply removing their proton is given in Figure S2 of the supplementary data for all ions in Figs. 4 and 5. These surfaces depict increasing electronegativity disparity, and therefore greater molecular bond dipole moments, in the sugar ring near the 2′-substituent from dNuo to Nuo to Nuofl molecules and ions. This increased disparity is depicted by the increasing electropositivity (dark blue) area in the sugar ring system near the highly electronegative (red) substituents of the ring. Ground structures for $[Cydfl+H]^+$ and $[Urdfl+H]^+$ were determined in this work, whereas those for $[Cyd+H]^+$, $[Urd+H]^+$, $[dCyd+H]^+$, and $[dUrd+H]^+$ are taken from previous work [40,43].

3.2.3. Vibration wavelength comparisons

Wavelength positioning of absorption bands are accurate, reproducible, and characteristic of specific vibrations in distinct chemical environments. The number and position of all absorption peaks in the $[Nuo+H]^+$ and $[dNuo+H]^+$ spectra are replicated in the spectra of $[Nuofl+H]^+$ for both pyrimidine nucleosides, suggesting similar gas-phase ion structures among these systems. Nearly all features exhibit increased yields, and certain features are more distinguishable from the baseline, e.g., features from ~1350–1450 cm^{-1}. In the hydrogen-stretching region, more O–H stretch absorption bands are observed between ~3600–3700 cm^{-1} for $[Cydfl+H]^+$ and $[Urdfl+H]^+$ compared to their $[Nuo+H]^+$ and $[dNuo+H]^+$ counterparts (see Figs. 4 and 5, respectively). These additional peaks result from the large electronegativity of the 2′-fluoro substituent altering the chemical environment of the nearby O3′–H stretch and thereby teasing apart absorption bands based on the sugar puckering adopted by the sugar that coalesced in the $[Nuo+H]^+$ and $[dNuo+H]^+$ action spectra. Vibrational modes for absorption bands, including the bands discussed in this section, are assigned for $[Cydfl+H]^+$ and $[Urdfl+H]^+$ in the supplementary data. The assignment and description of the three-dimensional gas-phase ion structures populated in the IRMPD experiments are provided primarily in Sections 3.4.1 and 3.4.2 of the main text.

3.3. Computational results

All unique and stable $[Cydfl+H]^+$ and $[Urdfl+H]^+$ structures computed are shown in Figures S3 and S4 of the supplementary

content, respectively. A graphical representation, conformer designation (including protonation site/tautomeric form), nucleobase orientation, sugar puckering, N1–C1′ glycosidic bond length, and relative B3LYP/6-311 + G(2d,2p) and MP2(full)/6311 + G(2d,2p) Gibbs energies at 298 K are given. Detailed descriptions of the $[Cydfl+H]^+$ and $[Urdfl+H]^+$ computed conformers are given in the text of the supplementary material. When rotations of functional groups produced multiple stable structures without any notable change in hydrogen-bonding interactions or chemical environment, the most stable structure was solely displayed as representative. Structures are designated based on the site of protonation (i.e., O2, N3, and O4) or minor tautomeric form (T) followed by a letter incremented alphabetically based on their relative B3LYP/6311 + G(2d,2p) Gibbs energies at 298 K. The nucleobase orientations are defined by the ∠C2N1C1′O4′ dihedral angle, where values between –90° and 90° are designated *syn* and values between 90° and 270° are designated *anti*. Sugar puckers were classified in two ways that have been described previously [39,41,42,44], including the common endo/exo designations [69,70] and the more descriptive designations based on sugar pseudorotation angle (*P*) [1]. The five dihedral angles of the sugar moiety are used to calculate *P*, which defines the structure with a two or three character sugar pucker description with one or two numbers and a letter (e.g. $^2T_3$, ^3E, $_3T^4$, etc.). In this nomenclature scheme, the letter represents either an envelope (E) or twist (T) conformation and the numbers before and after the letter represent the major and minor conformational motifs, respectively. Endo configurations are represented with superscripted numbers, whereas exo configurations are represented with subscripts.

3.3.1. B3LYP vs. MP2(full) energetics

Previous work, especially by Wu et al. and Zhu et al. [38–44,47], concluded that calculations at the B3LYP/6-311 + G(2d,2p) level of theory are especially robust and satisfactory for describing the protonated and sodium cationized forms of the canonical RNA and DNA nucleosides. However, MP2(full)/6-311 + G(2d,2p) energetics sometimes provide valuable ancillary information and insight. Highly parallel energetics are displayed in Table 1 for the major low-energy $[Nuofl+H]^+$ and counterpart canonical $[Nuo+H]^+$ and $[dNuo+H]^+$ systems. Therefore, in this work, the B3LYP/6-311 + G(2d,2p) Gibbs energies will be used in all discussions unless otherwise specifically noted to be the MP2(full)/6-311 + G(2d,2p) values.

3.3.2. Comparison of the $[Nuofl+H]^+$, $[Nuo+H]^+$, and $[dNuo+H]^+$ computed conformers

The preferred protonation sites are highly parallel amongst the $[Nuofl+H]^+$, $[Nuo+H]^+$, and $[dNuo+H]^+$ (see Table 1, Table 2, and Table S1) as the 2′position of the nucleosides is sufficiently physically and electronically isolated from the nucleobase to prohibit substantive impacts on the preferred protonation sites. For the Cyt series, B3LYP consistently suggests N3 protonation to be preferred by ~3 kJ/mol, whereas MP2(full) consistently suggests O2 protonation to be preferred by ~4 kJ/mol. For the Ura series, B3LYP predicts the 2,4-dihydroxy tautomer (T) and O4 protonated conformers to be competitive in stability, whereas MP2(full) predicts the 2,4-dihydroxy tautomer (T) to be preferred by ~9 kJ/mol. Both B3LYP and MP2(full) predict the most stable O2 protonated conformer to lie ~9 kJ/mol higher in Gibbs energy than the ground conformer.

The most common low-energy pyrimidine nucleobase orientations are *anti* orientations with ∠C2N1C1O4′ glycosidic bond angles of ~200° and ~226° with C3′-endo and C2′-endo sugar puckering, respectively (see e.g. the ground conformers of $[Cydfl+H]^+$, $[Cyd+H]^+$, $[dCyd+H]^+$, $[Urdfl+H]^+$, and $[dUrd+H]^+$ in Table 2 and Table S1). These *anti* nucleobase orientations, stabilized via noncanonical C6H···O5′H hydrogen bonds, are ubiquitous low-energy orientations for the protonated forms of the nucleosides. Protonation at the O2-position, including the 2,4-dihydroxy tautomer of the Ura systems, also allows the formation of an O2H···O5′H interaction that enhances stabilization of *syn* nucleobase orientations, with glycosidic bond angles of ~53°, to just ~3–10 kJ/mol above parallel *anti* orientations (e.g., **TC** and **O2A** of $[Urdfl+H]^+$, as well as **O2C** of $[Cydfl+H]^+$). Conformers lacking O2 protonation, i.e. N3 protonated Cyt nucleosides and O4 protonated Ura nucleosides, have *syn* orientations that lie ~23 kJ/mol higher in energy than their corresponding *anti* conformers (e.g., **O4G** of $[Urdfl+H]^+$ and **N3E** of $[Cydfl+H]^+$). In conformers with an available O2H hydrogen-bond donor, interactions with the hydrogen-bond accepting 2′-F and 2′-OH substituents allow the stabilization of *anti* nucleobase orientations with intermediate glycosidic bond angles of ~188°. The RNA analogues, with a 2′-OH, allow further stabilization of these conformers via bridging O2H···O2′H···O3′ interactions over the O2H···F2′···HO3′ interactions in 2′-F systems. The most stable structure with an ~188° glycosidic bond angle occurs in $[Urd+H]^+$ where **Ti** becomes the ground conformer by 0.2 kJ/mol over the more common ≥197° glycosidic bond angle *anti* orientation. The parallel $[Urdfl+H]^+$ conformer, **TE**, lies 19.4 kJ/mol above the ground conformer. In $[Cyd+H]^+$, **O2i**, containing a bridging O2H···O2′H···O3′ interaction, lies 5.8 kJ/mol above the ground conformer, whereas **N3ii**, containing an O3′H···O2′H···O2 interaction, lies 4.0 kJ/mol above the ground conformer. The parallel $[Cydfl+H]^+$ conformer, **O2G**, containing a dual O2H···F2′···HO3′ interaction, lies 24.7 kJ/mol above the ground conformer.

Tendencies regarding the preferred sugar puckering, C2′-endo vs. C3′-endo, across the 2′-substituents, 2′-F vs. 2′-OH vs. 2′-H, are not demonstrative of particularly strong stereoelectronic effects in the gas-phase. Energetics calculated with the B3LYP density functional suggest the ground $[Cydfl+H]^+$ and $[dUrd+H]^+$ to prefer C3′-endo sugar puckering by 0.7 and 0.4 kJ/mol, respectively, whereas the ground $[Cyd+H]^+$, $[dCyd+H]^+$, $[Urdfl+H]^+$, and $[Urd+H]^+$ prefer C2′endo

Table 1
Relative 0 and 298 K Enthalpies and 298 K Gibbs Energies of Major Conformers of $[Cydfl+H]^+$, $[Urdfl+H]^+$, $[Cyd+H]^+$, $[Urd+H]^+$, $[dCyd+H]^+$, and $[dUrd+H]^+$.[a,b]

Ion	Conformer	B3LYP			MP2(full)		
		ΔH_0	ΔH_{298}	ΔG_{298}	ΔH_0	ΔH_{298}	ΔG_{298}
$[Cydfl+H]^+$	**N3A**	0.0	0.0	0.0	5.0	5.4	4.9
	N3B	1.2	1.2	0.7	4.9	5.3	4.3
	O2A	2.6	2.2	2.7	0.0	0.0	0.0
	O2B	4.8	4.3	5.5	3.7	3.6	4.2
$[Urdfl+H]^+$	**TA**	0.0	0.0	0.0	0.0	0.9	0.0
	O4A	1.2	1.5	1.2	9.3	10.5	9.2
	O4B	3.2	3.6	2.5	10.1	11.4	9.5
	TB	2.8	2.8	3.3	4.4	5.3	5.0
$[Cyd+H]^+$	**N3A**	0.4	0.5	0.0	5.2	5.4	5.4
	N3i	0.0	0.0	0.6	5.0	5.4	5.4
	O2A	1.5	1.2	1.9	0.0	0.0	0.0
	O2B	3.9	3.5	4.4	2.7	2.7	3.0
$[Urd+H]^+$	**Ti**	0.0	0.0	0.0	0.0	0.0	0.0
	TA	1.0	2.2	0.2	1.2	2.4	0.3
	TB	3.4	4.6	2.5	4.1	5.4	3.2
	O4A	4.6	6.3	2.9	11.7	13.4	10.1
	O4i	3.5	5.0	3.0	10.7	12.1	10.1
$[dCyd+H]^+$	**N3A**	0.9	0.8	0.0	4.4	4.9	3.5
	N3B	0.0	0.0	0.2	5.4	5.9	3.5
	O2A	3.6	3.1	3.6	0.0	0.0	0.0
	O2B	4.4	4.0	5.2	3.0	3.1	3.8
$[dUrd+H]^+$	**O4B**	0.0	0.3	0.0	9.3	11.1	8.6
	O4A	1.9	2.1	0.4	9.7	11.5	7.4
	TA	0.9	0.7	0.7	0.9	2.3	0.0
	TB	1.2	1.1	1.7	3.5	5.0	3.3

[a] Energetics based on single-point energy calculations performed at the B3LYP/6-311 + G(2d,2p) and MP2(full)/6-311 + G(2d,2p) levels of theory with zero-point energy and thermal corrections based on the B3LYP/6-311 + G(d,p) optimized structures and vibrational frequencies.

[b] Results for $[Cyd+H]^+$ and $[dCyd+H]^+$ are taken from reference [40]. Results for $[Urd+H]^+$ and $[dUrd+H]^+$ are taken from reference [43].

Table 2
Geometric Parameters of the Most Stable Conformers Computed for $[Cydfl+H]^+$, $[Urdfl+H]^+$, $[Cyd+H]^+$, $[Urd+H]^+$, $[dCyd+H]^+$, and $[dUrd+H]^+$.[a]

Ion	Conformer	Nucleobase Orientation	Glycosidic Bond Length (Å)	Sugar Pucker	Hydrogen Bond	Hydrogen Bond Angle (°)	Hydrogen Bond Length (Å)
$[Cydfl+H]^+$	**N3A**	*anti*	1.516	C3′-endo ($^3T_2$)	∠O3′H···F	106.8	2.298
	N3B	*anti*	1.490	C2′-endo ($^2T_3$)	∠O3′H···F	98.1	2.415
	O2A	*anti*	1.495	C2′-endo ($^2T_3$)	∠O3′H···F	96.4	2.445
	O2B	*anti*	1.521	C3′-endo ($^3T_2$)	∠O3′H···F	106.3	2.306
$[Urdfl+H]^+$	**TA**	*anti*	1.503	C2′-endo ($^2T_3$)	∠O3′H···F	95.4	2.463
	O4A	*anti*	1.522	C3′-endo ($^3T_2$)	∠O3′H···F	106.5	2.304
	O4B	*anti*	1.497	C2′-endo ($^2T_3$)	∠O3′H···F	97.5	2.426
	TB	*anti*	1.530	C3′-endo ($^3T_2$)	∠O3′H···F	105.9	2.314
$[Cyd+H]^+$	**N3A**	*anti*	1.488	C2′-endo ($^2T_1$)	∠O2′H···O3′	112.5	2.159
	N3i	*anti*	1.522	C3′-endo ($^3T_2$)	∠O3′H···O2′	111.6	2.187
	O2A	*anti*	1.494	C2′-endo ($^2T_3$)	∠O2′H···O3′	113.7	2.135
	O2B	*anti*	1.524	C3′-endo (^3E)	∠O2′H···O3′	115.0	2.137
$[Urd+H]^+$	**Ti**	*anti*	1.508	C2′-endo ($^2T_3$)	∠O2′H···O3′	115.4	2.058
	TA	*anti*	1.502	C2′-endo ($^2T_3$)	∠O2′H···O3′	113.8	2.132
	TB	*anti*	1.533	C3′-endo (^3E)	∠O2′H···O3′	115.1	2.131
	O4A	*anti*	1.495	C2′-endo ($^2T_3$)	∠O2′H···O3′	112.4	2.162
	O4i	*anti*	1.528	C3′-endo ($^3T_2$)	∠O3′H···O2′	111.3	2.195
$[dCyd+H]^+$	**N3A**	*anti*	1.502	C2′-endo ($^2T_3$)	–	–	–
	N3B	*anti*	1.529	C3′-endo ($^3T_2$)	–	–	–
	O2A	*anti*	1.506	C2′-endo ($^2T_3$)	–	–	–
	O2B	*anti*	1.536	C3′-endo ($^3T_2$)	–	–	–
$[dUrd+H]^+$	**O4B**	*anti*	1.537	C3′-endo ($^3T_2$)	–	–	–
	O4A	*anti*	1.510	C2′-endo ($^2T_3$)	–	–	–
	TA	*anti*	1.514	C2′-endo ($^2T_3$)	–	–	–
	TB	*anti*	1.546	C3′-endo ($^3T_2$)	–	–	–

[a] Geometric details based on structures optimized at the B3LYP/6-311+G(d,p) level of theory. Results for $[Cyd+H]^+$ and $[dCyd+H]^+$ are taken from reference [40]. Results for $[Urd+H]^+$ and $[dUrd+H]^+$ are taken from reference [43].

sugar puckering by 0.6, 0.2, 1.2, and 2.5 kJ/mol, respectively. MP2(full) energetics, calculated with explicit treatment of electrons, consistently suggest C2′-endo sugar puckering to be preferred over, or equivalent with, C3′-endo sugar puckering in all systems. The MP2(full) ground conformers of $[Cydfl+H]^+$, $[Urdfl+H]^+$, $[Cyd+H]^+$, $[Urd+H]^+$, $[dCyd+H]^+$, and $[dUrd+H]^+$ prefer C2′endo sugar puckering by 4.2, 5.0, 3.0, 2.9, 3.8, and 3.3 kJ/mol, respectively. Thus, the MP2 results suggest C2′-endo sugar puckering to be increasingly preferred in the gas-phase following the order: 2′-OH < 2′-H < 2′-F. Overall, the results suggest C2′-endo sugar puckering, with ∠N1C1′C2′X2′ dihedral angles of ~83–91°, to generally be slightly preferred over C3′-endo sugar puckering, with ∠N1C1′C2′X2′ dihedral angles of ~145–150°, in the gas-phase pyrimidine $[Nuofl+H]^+$, $[Nuo+H]^+$, and $[dNuo+H]^+$.

To examine the effects of an implicit water solvent on the preferred sugar puckerings, calculations were also performed using the PCM on the same optimized conformers. In these PCM calculations, the B3LYP results suggest the ground $[Cydfl+H]^+$, $[Urdfl+H]^+$, $[Urd+H]^+$, and $[dUrd+H]^+$ to prefer C3′-endo sugar puckering by 2.4, 2.5, 1.5, and 0.5 kJ/mol, respectively, whereas the ground $[Cyd+H]^+$ and $[dCyd+H]^+$ prefer C2′-endo sugar puckering by 0.6 and 1.2 kJ/mol, respectively. The MP2(full) results from the PCM calculations suggest the ground $[Cydfl+H]^+$, $[Urdfl+H]^+$, and $[Urd+H]^+$ to prefer C3′-endo sugar puckering by 1.0, 0.5, and 0.6 kJ/mol, respectively, whereas the ground $[Cyd+H]^+$, $[dCyd+H]^+$, and $[dUrd+H]^+$ prefer C2′-endo sugar puckering by 0.5, 3.2, and 2.0 kJ/mol, respectively. Thus, the PCM calculations show an increasing number of systems, particularly the RNA and 2′-fluoronucleoside systems, preferring C3′-endo sugar puckering over C2′-endo sugar puckering relative to the gas-phase calculations. The following systems showed a change in preference from C2′-endo to C3′-endo in the PCM calculations relative to the gas-phase calculations: $[Urdfl+H]^+$ and $[Urd+H]^+$ in the B3LYP results, as well as $[Cydfl+H]^+$, $[Urdfl+H]^+$, and $[Urd+H]^+$ in the MP2(full) results. None of the DNA systems, with a 2′-H, showed a change in sugar puckering preference between the PCM and gas-phase calculations. These results suggest that the electronic properties of water generally aid in the stabilization of C3′-endo sugar puckerings in the RNA systems, with a 2′-OH, and 2′-fluoronucleosides, with a 2′-F, whereas the intrinsic properties of the DNA, RNA, and 2′-fluoronucleoside systems generally prefer C2′-endo sugar puckering in a solvent-free, gas-phase environment. The PCM results again suggest minimal stereoelectronic effects across the 2′-substituents, as evidenced by the small differences in Gibbs energies between the C2′-endo and C3′-endo sugar puckerings. Additionally, the experimental results herein suggest all systems to have a larger population of conformers with C2′-endo sugar puckering than C3′-endo, which is better represented by the gas-phase calculations than the PCM calculations. Ultimately, further work, such as natural bond order (NBO) analysis, is required to more rigorously and comprehensively examine the intrinsic effects of 2′-modifications on the preferred sugar puckering of nucleosides both in the gas-phase and in solution.

3.3.3. Hydrogen-bonding interactions of the sugar moieties

Overall the calculated structures for the protonated Nuofl nucleosides and previously studied canonical RNA and DNA nucleosides [40,43] are highly parallel (see Table 2 and Section 3.5.2), as expected due to the similar van der Waals radius of fluorine and hydrogen substituents [7], and the similarly high electronegativity leading to expectations of fairly similar gas-phase hydrogen-bond acceptance of fluorine and hydroxyl substituents. The number of stabile structure types increases from the DNA nucleosides to the 2′-fluoronucleosides to the RNA nucleosides due to increasing availability of intramolecular hydrogen-bonding interactions involving their 2′-substituents. The majority of $[Cydfl+H]^+$ and $[Urdfl+H]^+$ structures are stabilized by an O3′H···F2′ hydrogen-bonding interaction. These unidirectional interactions are similar to the bidirectional O3′H···O2′ and O2′H···O3′ hydrogen-bonding interactions found for $[Cyd+H]^+$ and $[Urd+H]^+$. Hydrogen-bonding interactions between the 2′- and 3′-substituents are not possible for $[dCyd+H]^+$ and $[dUrd+H]^+$ [40,43]. Table 2 includes geometric parameters related to the hydrogen bonding of the 2′- and 3′-substituents of the sugar moiety of the most stable calculated $[Cydfl+H]^+$, $[Urdfl+H]^+$, $[Cyd+H]^+$, and $[Urd+H]^+$ conformers. For Nuofl ions with C3′-endo ($^3T_2$) sugar puckering, the bound

∠O3′H···F2′ angle is ~107° and the hydrogen-bond length is ~2.31 Å. For the Nuofl ions with C2′-endo ($^2T_3$) sugar puckering, the bound ∠O3′H···F2′ angle is smaller at ~97°, and hydrogen-bond length is larger at ~2.44 Å. Thus, the calculations infer the hydrogen bonds involving fluorine to be stronger in protonated Nuofl with C3′-endo sugar puckering than C2′-endo puckering. In all cases, the hydrogen-bond length is calculated to be smaller than the sum of the fluorine and hydrogen van der Waals radii at 2.5–2.7 Å [2,7], providing further evidence for hydrogen-bonding interactions.

Additional evidence for the relative strengths of these hydrogen-bonding interactions involving fluorine comes from the magnitudes of the redshifts predicted for the O3′–H stretch in the C2′-endo and C3′-endo sugar puckered $[Cydfl+H]^+$ and $[Urdfl+H]^+$ conformers that exhibit an O3′H···F2′ hydrogen bond than those without this interaction. These predicted spectra can be found in Figures S5 and S6 of the supplementary material. Some analysis of spectral predictions compared with measured IRMPD spectra can be found in Sections 3.4.1 and 3.4.2, whereas more detailed comparisons can be found in the supplementary material. In $[Cydfl+H]^+$, the free O3′–H stretch of **N3C** and **O2D** are predicted at 3670 cm^{-1}. The O3′H···F2′ hydrogen-bonded O3′–H stretch of the C2′-endo ($^2T_3$) **O2A** and **N3B** conformers are predicted at 3646 cm^{-1}. The O3′H···F2′ hydrogen-bonded O3′–H stretch of the C3′-endo ($^3T_2$) **N3A** and **O2B** conformers are predicted at 3628 cm^{-1}. This O3′–H stretch was thus redshifted from the free O3′–H stretch by 24 and 42 cm^{-1} when hydrogen-bound to F2′ in C2′-endo and C3′-endo conformers of $[Cydfl+H]^+$, respectively. In $[Urdfl+H]^+$, the free O3′–H stretch of **O4C** and **TD** are predicted at 3658 cm^{-1}. The O3′H···F2′ hydrogen-bonded O3′–H stretch of C2′-endo ($^2T_3$) **TA** and **O4B** conformers are predicted at 3634 cm^{-1}. The O3′H···F2′ hydrogen-bonded O3′–H stretch of C3′-endo ($^3T_2$) **O4A** and **TB** conformers are predicted at 3615 cm^{-1}. The redshifts of this O3′–H stretch when hydrogen-bonded to F2′ in C2′-endo and C3′-endo conformers of $[Cydfl+H]^+$ are therefore 24 and 43 cm^{-1}, respectively, relative to the free O3′–H stretch. This trend, consistent for both $[Cydfl+H]^+$ and $[Urdfl+H]^+$, again indicates that the O3′H···F2′ hydrogen bonds are stronger in the C3′-endo ($^3T_2$) conformers than in the C2′-endo ($^2T_3$) conformers. However, all of these frequency shifts are fairly small indicating relatively weak hydrogen bonds.

In both C2′-endo ($^2T_3$) and C3′-endo ($^3T_2$) conformers of $[Cyd+H]^+$ and $[Urd+H]^+$, the ∠O3′H···O2′ and ∠O2′H···O3′ angles are nearer to linear and hydrogen-bonds shorter at ~113° and ~2.14 Å indicating a stronger interaction in comparison to the OH···F bonds. This assessment is in agreement with previous research, which concluded that OH···O interactions are seemingly stronger than OH···F interactions despite the higher electronegativity of fluorine over oxygen [2,11]. Because the O3′H···O2′ hydrogen bonds in $[Cyd+H]^+$ and $[Urd+H]^+$ are stronger than the O3′H···F2′ hydrogen bonds of $[Cydfl+H]^+$ and $[Urdfl+H]^+$, the $[Nuo+H]^+$ bound O3′–H hydrogen stretches exhibits red shifting of ~100 cm^{-1} relative to the free O3′–H stretch in the predicted and measured spectra. This red shifting causes coalescence of the bound O3′–H hydrogen stretch with the O–H^+ stretch of conformers protonated at a carbonyl.

In $[Cydfl+H]^+$, disruption of the **N3A** C3′-endo ($^3T_2$) O3′H···F2′ hydrogen bond by rotation of the ∠HC3′O3′H dihedral angle results in the 6.7 kJ/mol less stable **N3C** conformer after geometry optimization. Disruption of the O3′H···F2′ hydrogen bond of the **O2B** C3′-endo ($^3T_2$) conformer produces the **O2D** conformer that is 5.9 kJ/mol less stable. Rotating the ∠HC3′O3′H dihedral angle of $[Urdfl+H]^+$ to disrupt the O3′H···F2′ hydrogen bond of the C3′-endo ($^3T_2$) **O4A** and **TB** conformers creates the **O4C** and **TD** conformers, which are destabilized by 6.3 and 5.4 kJ/mol, respectively, after geometry optimization. Thus, engagement in the O3′H···F2′ hydrogen bond relaxes $[Cydfl+H]^+$ and $[Urdfl+H]^+$ structures with C3′-endo ($^3T_2$) sugar puckering by ~6 kJ/mol. These results are on par with the weak ~4–16 kJ/mol binding energies expected for fluorine acting as a hydrogen-bond acceptor [9]. C2′-endo ($^2T_3$) $[Cydfl+H]^+$ and $[Urdfl+H]^+$ structures always converged to form the O3′H···F2′ hydrogen-bonding interaction and therefore energy differences between hydrogen-bonded and non-hydrogen-bonded systems are unknown.

3.4. Experimental and theoretical spectral comparisons

Experimental $[Nuofl+H]^+$ IRMPD action spectra were compared with theoretical linear IR absorption spectra predicted for various stable conformers of $[Nuofl+H]^+$, vibrational modes were assigned to specific important experimental frequencies, and three-dimensional gas-phase ion structures were determined as having been populated in the experiments and ranked in importance based on their overall relative agreement with the B3LYP/6-311+G(d,p) predicted spectra and Gibbs energies at 298 K. The same vibrational scaling factors were applied as used previously for $[Nuo+H]^+$ and $[dNuo+H]^+$ [40,43].

3.4.1. $[Cydfl+H]^+$ spectral analysis and populated experimental conformers

Spectral comparisons for representative conformers of the 15 most-stable $[Cydfl+H]^+$ ions computed are provided in Figure S5 of the supplementary content. The majority of conformers exhibit spectral features that are consistent with the measured spectrum, and therefore cannot be excluded as possible minor components of the experimental gas-phase ion population. However, based on the computed relative stabilities and the overall higher degree of spectral matching it is deduced that the four most stable conformers (**N3A**, **N3B**, **O2A**, and **O2B**) and the structural characteristics that they represent are dominant and thus are chosen for display along with their nucleobase orientation, sugar puckering descriptions, and relative B3LYP/6-311+G(2d,2p) and MP2(full)/6-311+G(2d,2p) Gibbs energies at 298 K in Fig. 6. All four of these conformers have *anti* cytosine orientations and lie within a relatively small range of Gibbs energies, 5.5 kJ/mol. The primary structural difference between the A and B conformers of both the N3 and O2 protonated systems are their sugar puckers; **N3A** and **O2B** have C3′-endo puckering, whereas **N3B** and **O2A** exhibit C2′-endo puckering.

Comparisons between experimental and theoretical spectra are used as the basis for determining the structures populated in the gas phase. Good agreement between experiment and theory is typically found [68]. The features observed here in the measured IRMPD spectrum of $[Cydfl+H]^+$ require multiple structures to have been present to account for all of the significant absorption bands. Overall, theory predicted the number of bands well in all spectral regions, and band positions are predicted quite well in the fingerprint region with some minor shifting in the hydrogen-stretching region. The most significant difference observed is a 15 cm^{-1} redshift of the O2–H stretch of the O2 protonated conformers (**O2A** and **O2B**), predicted at 3595 cm^{-1} and measured at 3580 cm^{-1}. These peak shifts can be explained by the expected higher anharmonicity due to the localized charge of the O2–H stretching mode in the multiple-photon IRMPD process compared with the predicted single-photon IR absorption spectra of an O—H stretch without localized charge [68,71–74]. Although single scale factors were chosen to best represent the individual fingerprint and hydrogen-stretching regions, each vibrational mode may exhibit a different level of anharmonicity and therefore spectral shifts must naturally be expected. Theory seems to significantly underestimate the intensity of absorption bands in the ~700–1425 cm^{-1} range of the fingerprint region.

Details of the $[Cydfl+H]^+$ spectral analyses are given in the supplementary material. In summary, N3 and O2 protonated conformers of $[Cydfl+H]^+$ are approximately equally populated as gas-phase ions in the experiments. The Cyt nucleobase preferentially adopts the lower-energy *anti* orientation stabilized by a noncanonical C6H···O5′ hydrogen bond, although higher energy *syn* conformers could not be ruled out as minor contributors to the population. Both C2′-endo ($^2T_3$) and C3′-endo ($^3T_2$) sugar-puckered conformers are among the experimental population, with the majority being C2′-endo. However, as explained

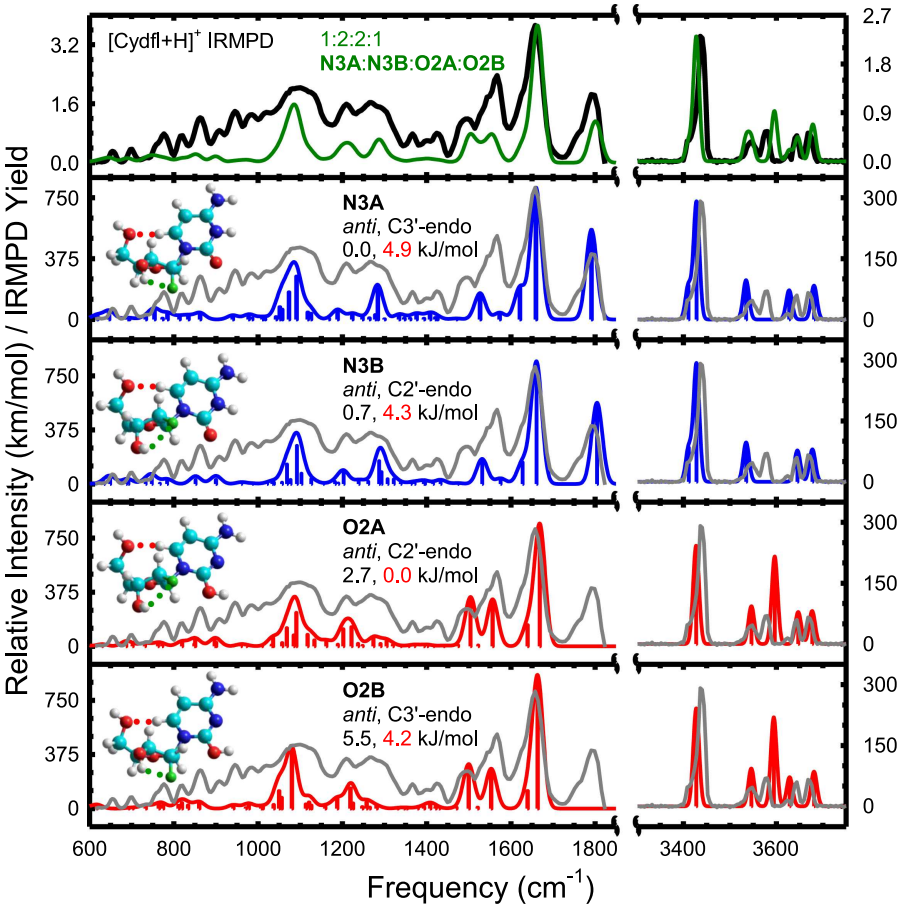

Fig. 6. Comparisons of the experimental IRMPD action spectrum of $[Cydfl+H]^+$ (shown in black in the top panel and overlaid in grey and scaled to match the most intense feature in each region in all other panels) with the theoretical linear IR spectra predicted for the four most stable conformations of $[Cydfl+H]^+$ (shown in blue for N3 protonated conformers and in red for O2 protonated conformers in the bottom four panels). The optimized structure, conformer designation, nucleobase orientation, sugar puckering designation, and B3LYP/6-311+G(2d,2p) (shown in black) and MP2(full)/6311+G(2d,2p) (shown in red) relative Gibbs energy at 298 K are given. The predicted IR spectrum for a 1:2:2:1 mixture of the **N3A**, **N3B**, **O2A**, and **O2B** conformers, respectively, is overlaid in green in the top panel (For interpretation of the references to colour in this figure legend, the reader is referred to the web version of this article).

previously, the extent of C2′-endo dominance over C3′-endo is unknown due to the greater 3′OH···F2′ hydrogen-bond strength of C3′-endo structures than C2′-endo structures, which could possibly dampen the C3′-endo 3′OH···F2′ hydrogen-stretch response in the IRMPD spectrum. The bands measured at 3625 and 3645 cm^{-1} could not be reasonably explained in the absence of 3′OH···F2′ hydrogen bonds. These conclusions are solidified by the high degree of similarity in both the relative intensity and spectral alignment of the features in the top panel of Fig. 6, which compares an averaged theoretical spectrum with a 2:1 ratio of C2′-endo ($^2T_3$) to C3′-endo ($^3T_2$) sugar puckers for both O2 and N3 protonated conformers, i.e., for a 1:2:2:1 **N3A**:**N3B**:**O2A**:**O2B** mixture.

3.4.2. $[Urdfl+H]^+$ spectral analysis and populated experimental conformers

Spectral comparisons for representative conformers of the 15 most stable $[Urdfl+H]^+$ conformers computed are provided in Figure S6 of the supplementary material. Most conformers display spectral features that correspond well with the experimental spectrum and therefore cannot be excluded as minor contributors to the experimental population. However, based on their computed relative stabilities and overall higher degree of spectral matching, the four lowest energy conformers (**TA**, **O4A**, **O4B**, and **TB**) and the structural features that they represent are dominant and chosen for display in Fig. 7. The Ura orientation is *anti* for these conformers. The primary structural difference between the A and B designations of the 2,4-dihydroxy tautomer (T) and O4 protonation motifs are the puckering of the sugar moiety, C2′-endo or C3′-endo. All four conformers have B3LYP/6311+G(2d,2p) Gibbs energies at 298 K within 3.3 kJ/mol of **TA**, the ground conformer.

Details of the $[Urdfl+H]^+$ spectral analysis are given in the supplementary material. In summary, T conformers dominate the experimental population, but are accompanied by a significant presence of O4 protonated conformers. O2 protonated conformers if present are only populated in very minor abundance. The Ura nucleobase preferentially adopts an *anti* orientation, although *syn* conformers cannot be excluded as minor contributors to the experimental population. Significant evidence of O3′H···F2′ hydrogen-bonding interactions partially explains the absorption bands at 3605 and 3640 cm^{-1}. The puckering of the sugar moiety of the conformers present is both C2′-endo ($^2T_3$) and C3′-endo ($^3T_2$), with the latter present in lesser amount. However, as explained in Section 3.4.1. for $[Cydfl+H]^+$, the geometric data in Table 2 suggests that the O3′H···F2′ hydrogen bond is stronger in C3′-endo than in C2′-endo conformers, which could dampen its IR absorption and IRMPD yield. The top panel of Fig. 7 displays a high degree of spectral matching between the measured IRMPD spectrum and an average theoretical spectrum dominated by **TA**, a 2,4-dihydroxy tautomer with an *anti* nucleobase orientation and C2′-endo ($^2T_3$) sugar puckering, by combining a 3:1:1:1 mixture of **TA**:**O4A**:**O4B**:**TB**, respectively. Based on these results, the relative abundance of 2,4-dihydroxy tautomers of $[Urdfl+H]^+$ is estimated as ~70% of the experimental population.

3.5. Comparisons of the experimentally-populated pyrimidine $[Nuofl+H]^+$, $[Nuo+H]^+$, and $[dNuo+H]^+$

3.5.1. Glycosidic bond lengths and stabilities

Survival yield analyses of the protonated pyrimidine nucleosides indicate that the N1–C1′ glycosidic bond stability increases from 2′-H to 2′-OH to 2′-F substituents (see Fig. 3 and Section 3.1.2). This trend in glycosidic bond stability is consistent with the theoretical N1–C1′ bond lengths. The general trend displayed in Table 2 for the dominantly populated low-energy conformers for the pyrimidine $[Nuofl+H]^+$,

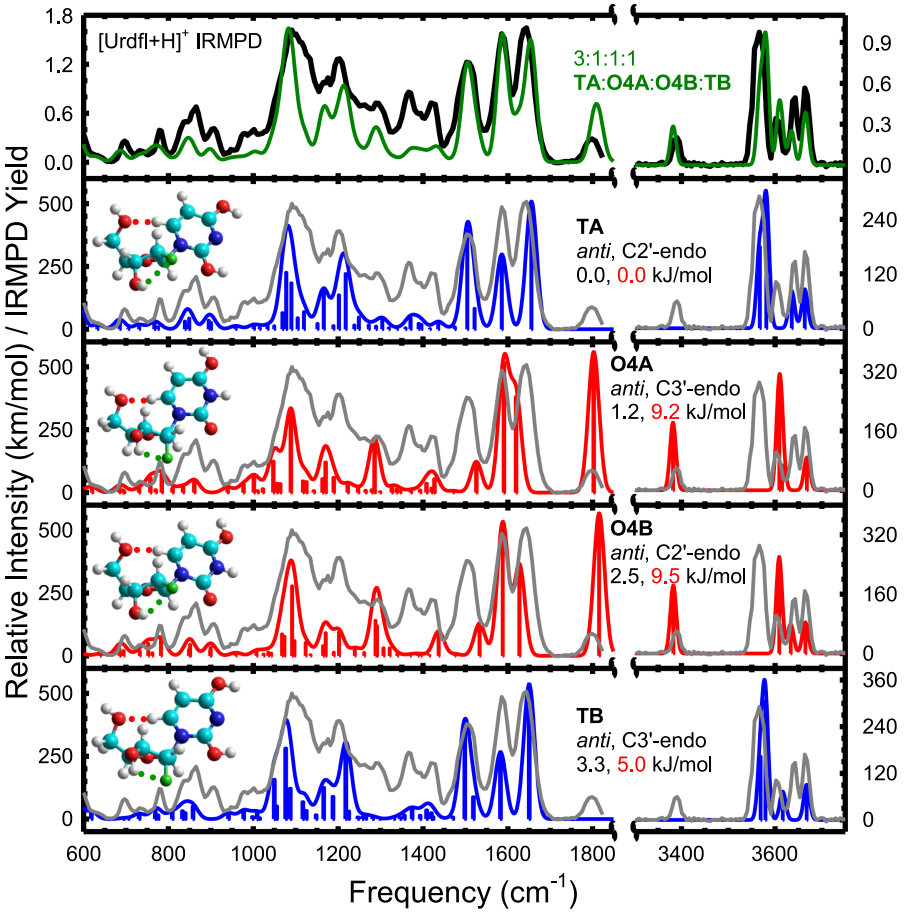

Fig. 7. Comparisons of the experimental IRMPD action spectrum of $[Urdfl+H]^+$ (shown in black in the top panel and overlaid in grey and scaled to match the most intense feature in each region in all other panels) with the theoretical linear IR spectra predicted for the four most stable conformations of $[Urdfl+H]^+$ (shown in blue for minor tautomer conformers and in red for O4 protonated conformers in the bottom four panels). The optimized structure, conformer designations, nucleobase orientation, sugar puckering designation, and B3LYP/6-311+G(2d,2p) (shown in black) and MP2(full)/6311+G(2d,2p) (shown in red) relative Gibbs energy at 298 K are given. The predicted IR spectrum for a 3:1:1:1 mixture of **TA**, **O4A**, **TB**, and **O4B** conformers, respectively, is overlaid in green in the top panel (For interpretation of the references to colour in this figure legend, the reader is referred to the web version of this article).

$[Nuo+H]^+$, and $[dNuo+H]^+$ systems shows a generally increasing N1–C1′ bond distance with decreasing 2′-substituent electronegativity. The average (and standard deviation) of the bond lengths for each protonated nucleoside is as follows: $[Cydfl+H]^+$ 1.506 (0.015); $[Cyd+H]^+$ 1.507 (0.002); $[dCyd+H]^+$ 1.518 (0.017); $[Urdfl+H]^+$ 1.513 (0.016), $[Urd+H]^+$ 1.513 (0.002) and $[dUrd+H]^+$ 1.527 (0.018). Thus, theory indicates that the glycosidic bond of $[dCyd+H]^+$ shrinks by ~0.014 Å versus $[Cyd+H]^+$, whereas the glycosidic bond of $[dUrd+H]^+$ shrinks by ~0.011 Å versus $[Urd+H]^+$. The minimal to no decrease in the N1–C1′ bond length from $[Nuo+H]^+$ to $[Nuofl+H]^+$ would suggest similar glycosidic bond strengths, but the survival yield experiments clearly show an increase in $CID_{50\%}$ of approximately the same magnitude as that between $[dNuo+H]^+$ and $[Nuo+H]^+$ (see Fig. 3) suggesting that the enhanced glycosidic bond strength of the 2′-fluoronucleosides is associated with the greater reluctance of the 2′-fluorinated sugar to give up its 2′-hydrogen to the departing nucleobase.

3.5.2. Major populated structures

Comparison of the overall structural motifs and conformers populated in the IRMPD action spectroscopy experiments presented here to those for the counterpart $[Nuo+H]^+$ and $[dNuo+H]^+$ systems [40,43] show that the 2′-substituent, whether it be H, OH, or F, does not markedly impact the structure or stability of these protonated pyrimidine nucleosides (see Figures S7 and S8). To summarize, diverse mixtures of $[Urdfl+H]^+$, $[Urd+H]^+$, and $[dUrd+H]^+$ are potentially accessed in the experiments, but the populations are dominated by 2,4-dihydroxy tautomers followed by O4 protonated conformers, comprising roughly ~70% and ~30% of the experimental populations, respectively. The Ura nucleobase preferentially adopts an *anti* orientation over *syn* in all three types of nucleosides. This conclusion is further supported by single point energy calculations where the *anti* conformers exhibit greater computed stability than the *syn* conformers. In $[Urdfl+H]^+$, C2′-endo ($^2T_3$) sugar puckering is determined to be dominant over C3′-endo ($^3T_2$), but the relative sugar-pucker populations could not be distinguished in $[Urd+H]^+$ and $[dUrd+H]^+$. For the $[Cydfl+H]^+$, $[Cyd+H]^+$, and $[dCyd+H]^+$ systems, spectral and theoretical evidence suggests both N3 and O2 protonated conformations coexist in approximately equal amounts in the experimental population in all cases. In all systems the nucleobase heavily prefers an *anti* orientation over *syn*. The experimental populations are dominated by C2′-endo puckered conformers in all three systems with C3′-endo conformers existing as a significant, but minor, component of the populations.

4. Conclusions

Results for $[Cydfl+H]^+$ and $[Urdfl+H]^+$ are reported here and compared to previous work on $[Cyd+H]^+$, $[Urd+H]^+$, $[dCyd+H]^+$, and $[dUrd+H]^+$ [38–44,47]. Collisionally activated unimolecular dissociation of protonated Cydfl proceeds only through *N*-glycosidic bond cleavage with retention of the proton by the Cyt nucleobase. Fragmentation of $[Urdfl+H]^+$ proceeds primarily through parallel *N*-glycosidic bond cleavage, but additional ketene and water loss pathways are also observed based on fragment ion *m/z*. ER-CID survival yield experiments are performed to determine relative N1–C1′ glycosidic bond strengths. The rf excitation energy that produced 50% precursor ion fragmentation is used as a measure of the relative glycosidic bond stability. Protonated nucleosides with a Cyt nucleobase are found to have higher glycosidic bond strength than those with Ura. The relative glycosidic bond stabilities for protonated nucleosides with different 2′-substituents follows the order of 2′-F > 2′-OH > 2′-H. IRMPD action spectra measured from ~600 to 1850 cm^{-1} and 3300 to 3800 cm^{-1}

compared to B3LYP/6-311 + G(d,p) predicted linear IR spectra allow for the determination of experimentally accessed gas-phase ion structures. Overall, the $[Nuofl+H]^+$ populated structures are found to be highly parallel to those populated for the $[Nuo+H]^+$ and $[dNuo+H]^+$ systems. The 2′-fluorine substituent increases the IR absorption efficiency and IRMPD yields relative to the canonical DNA and RNA nucleosides. $[Cydfl+H]^+$ is protonated in approximately similar abundance at both the O2 and N3 positions. The major $[Urdfl+H]^+$ protonation motif is a 2,4-dihydroxy minor tautomer, followed by the lesser populated O4 protonated canonical tautomer, followed finally by non- or minimally-populated O2 protonated conformers. $[Cydfl+H]^+$ and $[Urdfl+H]^+$ systems both preferentially adopt *anti* nucleobase orientations stabilized by a noncanonical C6H···O5′ hydrogen bond, although conformers with a *syn* nucleobase orientation may possibly be populated to a minor degree. C2′-endo ($^2T_3$) is the major sugar puckering, but C3′-endo ($^3T_2$) conformers are populated to a significant yet lesser degree. Evidence for gas-phase intramolecular O3′H···F2′ hydrogen-bonding interactions is found in the hydrogen-stretching region of the $[Nuofl+H]^+$ IRMPD action spectra. The increased glycosidic bond strengths, increased IRMPD yields, and capability for differentiation of OH stretches from C2′-endo and C3′-endo sugar-puckered nucleosides are attributed to the electronic effects of the maximally electronegative 2′-fluoro substituent. These results support several of the primary reasons for use of fluorine in biological chemistry: minimal perturbation of molecular structures, hydrogen-bond acceptance, and substantial electronic chemical effects [15].

Acknowledgements

This work was supported by the National Science Foundation grant numbers OISE-1357887 for the international travel and IRMPD experiments, DBI-0922819 for the Bruker amaZon ETD QIT mass spectrometer used in this work, and CHE-1709789 for all other research costs. Z.J.D., C.C.H., Y.Z., and L.A.H. gratefully acknowledge support from the Wayne State University Thomas C. Rumble Fellowship. Z.J.D. gratefully acknowledges support from the Wayne State University Joseph Jasper Scholarship for Graduate Students in Chemistry. The authors would also like to thank WSU C&IT for computer time and support. We gratefully acknowledge the Nederlandse Organisatie voor Wetenschappelijk Onderzoek (NWO) for the support of the FELIX Laboratory. The authors are exceedingly appreciative of the skillful assistance of the FELIX staff.

Appendix A. Supplementary data

Supplementary material related to this article can be found, in the online version, at doi:https://doi.org/10.1016/j.jfluchem.2018.12.004.

References

[1] M. Egli, W. Saenger, Principles of Nucleic Acid Structure, Springer Science & Business Media, 1984.
[2] L. Pauling, The Nature of the Chemical Bond and the Structure of Molecules and Crystals: An Introduction to Modern Structural Chemistry, Cornell University Press, 1960.
[3] W.K. Hagmann, The many roles for fluorine in medicinal chemistry, J. Med. Chem. 51 (2008) 4359–4369.
[4] D. O'Hagan, Understanding organofluorine chemistry: An introduction to the C-F bond, Chem. Soc. Rev. 37 (2008) 308–319.
[5] B.E. Smart, Fluorine substituent effects (on bioactivity), J. Fluorine Chem. 109 (2001) 3–11.
[6] J.A.K. Howard, V.J. Hoy, D. O'Hagan, G.T. Smith, How good is fluorine as a hydrogen bond acceptor? Tetrahedron 52 (1996) 12613–12622.
[7] A. Bondi, van der Waals volumes and radii, J. Phys. Chem. 68 (1964) 441–451.
[8] L. Brammer, E.A. Bruton, P. Sherwood, Understanding the behavior of halogens as hydrogen bond acceptors, Cryst. Growth Des. 1 (2001) 277–290.
[9] P.A. Champagne, J. Desroches, J.-F. Paquin, Organic fluorine as a hydrogen-bond acceptor: Recent examples and applications, Synthesis 47 (2015) 306–322.
[10] C. Dalvit, C. Invernizzi, A. Vulpetti, Fluorine as a hydrogen-bond acceptor: Experimental evidence and computational calculations, Chem. Eur. J. 20 (2014) 11058–11068.
[11] J.D. Dunitz, R. Taylor, Organic fluorine hardly ever accepts hydrogen bonds, Chem. Eur. J. 3 (1997) 89–98.
[12] G.T. Giuffredi, V. Gouverneur, B. Bernet, Intramolecular OH···FC hydrogen bonding in fluorinated carbohydrates: CHF is a better hydrogen bond acceptor than CF_2, Angew. Chem. Int. Ed. 52 (2013) 10524–10528.
[13] H.-J. Schneider, Hydrogen bonds with fluorine: Studies in solution, in gas phase and by computations, conflicting conclusions from crystallographic analyses, Chem. Sci. 3 (2012) 1381–1394.
[14] C. Shugrue, J. DeFrancisco, A. Metrano, B. Brink, R. Nomoto, B. Linton, Detection of weak hydrogen bonding to fluoro and nitro groups in solution using H/D exchange, Org. Biomol. Chem. 14 (2016) 2223–2227.
[15] S. Purser, P.R. Moore, S. Swallow, V. Gouverneur, Fluorine in medicinal chemistry, Chem. Soc. Rev. 37 (2008) 320–330.
[16] J.-P. Bégué, D. Bonnet-Delpon, Recent advances (1995–2005) in fluorinated pharmaceuticals based on natural products, J. Fluorine Chem. 127 (2006) 992–1012.
[17] H.J. Böhm, D. Banner, S. Bendels, M. Kansy, B. Kuhn, K. Müller, U. Obst-Sander, M. Stahl, Fluorine in medicinal chemistry, Chem. Bio. Chem. 5 (2004) 637–643.
[18] R. Filler, R. Saha, Fluorine in medicinal chemistry: A century of progress and a 60-year retrospective of selected highlights, Future Med. Chem. 1 (2009) 777–791.
[19] E.P. Gillis, K.J. Eastman, M.D. Hill, D.J. Donnelly, N.A. Meanwell, Applications of fluorine in medicinal chemistry, J. Med. Chem. 58 (2015) 8315–8359.
[20] C. Isanbor, D. O'Hagan, Fluorine in medicinal chemistry: A review of anti-cancer agents, J. Fluorine Chem. 127 (2006) 303–319.
[21] F.M. Ismail, Important fluorinated drugs in experimental and clinical use, J. Fluorine Chem. 118 (2002) 27–33.
[22] K.L. Kirk, Fluorine in medicinal chemistry: Recent therapeutic applications of fluorinated small molecules, J. Fluorine Chem. 127 (2006) 1013–1029.
[23] K.L. Kirk, Fluorination in medicinal chemistry: Methods, strategies, and recent developments, Org. Process Res. Dev. 12 (2008) 305–321.
[24] K. Müller, C. Faeh, F. Diederich, Fluorine in pharmaceuticals: Looking beyond intuition, Science 317 (2007) 1881–1886.
[25] P. Shah, A.D. Westwell, The role of fluorine in medicinal chemistry, J. Enzyme Inhib. Med. Chem. 22 (2007) 527–540.
[26] D. O'Hagan, Fluorine in health care: Organofluorine containing blockbuster drugs, J. Fluorine Chem. 131 (2010) 1071–1081.
[27] C. Heidelberger, N.K. Chaudhuri, P. Danneberg, D. Mooren, L. Griesbach, R. Duschinsky, R.J. Schnitzer, E. Pleven, J. Scheiner, Fluorinated pyrimidines, a new class of tumour-inhibitory compounds, Nature 179 (1957) 663–666.
[28] W. Plunkett, P. Huang, Y.-Z. Xu, V. Heinemann, R. Grunewald, V. Gandhi, Gemcitabine: Metabolism, mechanisms of action, and self-potentiation, Semin. Oncol. 22 (1995) 3–10.
[29] J.L. Grem, 5-Fluorouracil: Forty-plus and still ticking. A review of its preclinical and clinical development, Invest. New Drugs 18 (2000) 299–313.
[30] B. Clarkson, A. O'Connor, L. Winston, D. Hutchison, The physiologic disposition of 5-fluorouracil and 5-fluoro-2′-deoxyuridine in man, Clin. Pharmacol. Ther. 5 (1964) 581–610.
[31] S.G. Lim, T.M. Ng, N. Kung, Z. Krastev, M. Volfova, P. Husa, S.S. Lee, S. Chan, M.L. Shiffman, M.K. Washington, A double-blind placebo-controlled study of emtricitabine in chronic hepatitis B, Arch. Intern. Med. 166 (2006) 49–56.
[32] World Health Organization, WHO Model List of Essential Medicines, (2017).
[33] C.M. Kaczan, A.I. Rathur, R.R. Wu, Y. Chen, C.A. Austin, G. Berden, J. Oomens, M.T. Rodgers, Infrared multiple photon dissociation action spectroscopy of sodium cationized halouracils: Effects of sodium cationization and halogenation on gas-phase conformation, Int. J. Mass Spectrom. 378 (2015) 76–85.
[34] Y.-w. Nei, T.E. Akinyemi, C.M. Kaczan, J.D. Steill, G. Berden, J. Oomens, M.T. Rodgers, Infrared multiple photon dissociation action spectroscopy of sodiated uracil and thiouracils: Effects of thioketo-substitution on gas-phase conformation, Int. J. Mass Spectrom. 308 (2011) 191–202.
[35] B. Yang, R.R. Wu, G. Berden, J. Oomens, M.T. Rodgers, Infrared multiple photon dissociation action spectroscopy of proton-bound dimers of cytosine and modified cytosines: Effects of modifications on gas-phase conformations, J. Phys. Chem. B 117 (2013) 14191–14201.
[36] B. Yang, R.R. Wu, N.C. Polfer, G. Berden, J. Oomens, M.T. Rodgers, IRMPD action spectroscopy of alkali metal cation–cytosine complexes: Effects of alkali metal cation size on gas phase conformation, J. Am. Soc. Mass Spectrom. 24 (2013) 1523–1533.
[37] T.E. Akinyemi, R.R. Wu, Y.-w. Nei, N.A. Cunningham, H.A. Roy, J.D. Steill, G. Berden, J. Oomens, M.T. Rodgers, Influence of transition metal cationization versus sodium cationization and protonation on the gas-phase tautomeric conformations of uracil: Application to $[Ura+Cu]^+$ and $[Ura+Ag]^+$, J. Am. Soc. Mass Spectrom 28 (2017) 2438–2453.
[38] R.R. Wu, B. Yang, G. Berden, J. Oomens, M.T. Rodgers, Gas-phase conformations and energetics of protonated 2′-deoxyadenosine and adenosine: IRMPD action spectroscopy and theoretical studies, J. Phys. Chem. B 119 (2015) 2795–2805.
[39] Y. Zhu, L.A. Hamlow, C.C. He, S.F. Strobehn, J.K. Lee, J. Gao, G. Berden, J. Oomens, M.T. Rodgers, Influence of sodium cationization versus protonation on the gas-phase conformations and glycosidic bond stabilities of 2′-deoxyadenosine and adenosine, J. Phys. Chem. B 120 (2016) 8892–8904.
[40] R.R. Wu, B. Yang, C.E. Frieler, G. Berden, J. Oomens, M.T. Rodgers, N3 and O2 protonated tautomeric conformations of 2′-deoxycytidine and cytidine coexist in the gas phase, J. Phys. Chem. B 119 (2015) 5773–5784.
[41] Y. Zhu, L.A. Hamlow, C.C. He, H.A. Roy, N.A. Cunningham, M. Munshi, G. Berden, J. Oomens, M.T. Rodgers, Conformations and N-glycosidic bond stabilities of sodium cationized 2′-deoxycytidine and cytidine: Solution conformation of $[Cyd+Na]^+$ is preserved upon ESI, Int. J. Mass Spectrom. 429 (2018) 18–27.

[42] Y. Zhu, L.A. Hamlow, C.C. He, J.K. Lee, J. Gao, G. Berden, J. Oomens, M.T. Rodgers, Gas-phase conformations and N-glycosidic bond stabilities of sodium cationized 2′-deoxyguanosine and guanosine: Sodium cations preferentially bind to the guanine residue, J. Phys. Chem. B 121 (2017) 4048–4060.
[43] R.R. Wu, B. Yang, C.E. Frieler, G. Berden, J. Oomens, M.T. Rodgers, Diverse mixtures of 2,4-dihydroxy tautomers and O4 protonated conformers of uridine and 2′-deoxyuridine coexist in the gas phase, Phys. Chem. Chem. Phys. 17 (2015) 25978–25988.
[44] Y. Zhu, H.A. Roy, N.A. Cunningham, S.F. Strobehn, J. Gao, M.U. Munshi, G. Berden, J. Oomens, M.T. Rodgers, Effects of sodium cationization versus protonation on the conformations and N-glycosidic bond stabilities of sodium cationized uridine and 2′-deoxyuridine: Solution conformation of $[Urd+Na]^+$ is preserved upon ESI, Phys. Chem. Chem. Phys. 19 (2017) 17637–17652.
[45] A. Filippi, C. Fraschetti, F. Rondino, S. Piccirillo, V. Steinmetz, L. Guidoni, M. Speranza, Protonated pyrimidine nucleosides probed by IRMPD spectroscopy, Int. J. Mass Spectrom. 354 (2013) 54–61.
[46] H.U. Ung, K.T. Huynh, J.C. Poutsma, J. Oomens, G. Berden, T.H. Morton, Investigation of proton affinities and gas phase vibrational spectra of protonated nucleosides, deoxynucleosides, and their analogs, Int. J. Mass Spectrom. 378 (2015) 294–302.
[47] R.R. Wu, B. Yang, G. Berden, J. Oomens, M.T. Rodgers, Gas-phase conformations and energetics of protonated 2′-deoxyguanosine and guanosine: IRMPD action spectroscopy and theoretical studies, J. Phys. Chem. B 118 (2014) 14774–14784.
[48] M.R. Ligare, A.M. Rijs, G. Berden, M. Kabeláč, D. Nachtigallova, J. Oomens, M.S. de Vries, Resonant infrared multiple photon dissociation spectroscopy of anionic nucleotide monophosphate clusters, J. Phys. Chem. B 119 (2015) 7894–7901.
[49] Y.-w. Nei, K.T. Crampton, G. Berden, J. Oomens, M.T. Rodgers, Infrared multiple photon dissociation action spectroscopy of deprotonated RNA mononucleotides: Gas-phase conformations and energetics, J. Phys. Chem. A 117 (2013) 10634–10649.
[50] Y.-w. Nei, N. Hallowita, J.D. Steill, J. Oomens, M.T. Rodgers, Infrared multiple photon dissociation action spectroscopy of deprotonated DNA mononucleotides: Gas-phase conformations and energetics, J. Phys. Chem. A 117 (2013) 1319–1335.
[51] R.R. Wu, C.C. He, L.A. Hamlow, Y.-w. Nei, G. Berden, J. Oomens, M.T. Rodgers, Protonation induces base rotation of purine nucleotides pdGuo and pGuo, Phys. Chem. Chem. Phys. 18 (2016) 15081–15090.
[52] R.R. Wu, C.C. He, L.A. Hamlow, Y.-w. Nei, G. Berden, J. Oomens, M.T. Rodgers, N3 protonation induces base rotation of 2′-deoxyadenosine-5′-monophosphate and adenosine-5′-monophosphate, J. Phys. Chem. B 120 (2016) 4616–4624.
[53] F. Derwa, E. De Pauw, P. Natalis, New basis for a method for the estimation of secondary ion internal energy distribution in 'soft' ionization techniques, J. Mass Spectrom. 26 (1991) 117–118.
[54] X. Guo, M.C. Duursma, P.G. Kistemaker, N.M. Nibbering, K. Vekey, L. Drahos, R. Heeren, Manipulating internal energy of protonated biomolecules in electrospray ionization Fourier transform ion cyclotron resonance mass spectrometry, J. Mass Spectrom. 38 (2003) 597–606.
[55] T.M. Kertesz, L.H. Hall, D.W. Hill, D.F. Grant, CE 50: Quantifying collision induced dissociation energy for small molecule characterization and identification, J. Am. Soc. Mass Spectrom. 20 (2009) 1759–1767.
[56] A. Memboeuf, L. Jullien, R. Lartia, B. Brasme, Y. Gimbert, Tandem mass spectrometric analysis of a mixture of isobars using the survival yield technique, J. Am. Soc. Mass Spectrom. 22 (2011) 1744–1752.
[57] A. Memboeuf, A. Nasioudis, S. Indelicato, F. Pollreisz, A. Kuki, S. Kéki, O.F. van den Brink, K. Vékey, L. Drahos, Size effect on fragmentation in tandem mass spectrometry, Anal. Chem. 82 (2010) 2294–2302.
[58] J.J. Valle, J.R. Eyler, J. Oomens, D.T. Moore, A.F.G. van der Meer, G. von Helden, G. Meijer, C.L. Hendrickson, A.G. Marshall, G.T. Blakney, Free electron laser-fourier transform ion cyclotron resonance mass spectrometry facility for obtaining infrared multiphoton dissociation spectra of gaseous ions, Rev. Sci. Instrum. 76 (2005) 023103.
[59] S. Guan, A.G. Marshall, Stored waveform inverse Fourier transform (SWIFT) ion excitation in trapped-ion mass spectometry: Theory and applications, Int. J. Mass Spectrom. Ion Process. 157 (1996) 5–37.
[60] K.K. Lehmann, G. Scoles, B.H. Pate, Intramolecular dynamics from eigenstate-resolved infrared spectra, Annu. Rev. Phys. Chem. 45 (1994) 241–274.
[61] M. Almasian, J. Grzetic, J. van Maurik, J.D. Steill, G. Berden, S. Ingemann, W.J. Buma, J. Oomens, Non-equilibrium isomer distribution of the gas-phase photoactive yellow protein chromophore, J. Phys. Chem. Lett. 3 (2012) 2259–2263.
[62] HyperChem Computational Chemistry Software Package, Version 5.0, Hypercube Inc., Gainesville, FL, United States, 1997.
[63] M.J. Frisch, G.W. Trucks, H.B. Schlegel, G.E. Scuseria, M.A. Robb, J.R. Cheeseman, et al., Gaussian 09, Revision E.01, Gaussian, Inc., Wallingford, CT, 2009.
[64] J.P. Merrick, D. Moran, L. Radom, An evaluation of harmonic vibrational frequency scale factors, J. Phys. Chem. A 111 (2007) 11683–11700.
[65] R.E. March, Quadrupole ion traps, Mass Spectrom. Rev. 28 (2009) 961–989.
[66] M.T. Bennett, M.T. Rodgers, A.S. Hebert, L.E. Ruslander, L. Eisele, A.C. Drohat, Specificity of human thymine DNA glycosylase depends on N-glycosidic bond stability, J. Am. Chem. Soc. 128 (2006) 12510–12519.
[67] B. Ewald, D. Sampath, W. Plunkett, Nucleoside analogs: Molecular mechanisms signaling cell death, Oncogene 27 (2008) 6522–6537.
[68] J. Oomens, B.G. Sartakov, G. Meijer, G. Von Helden, Gas-phase infrared multiple photon dissociation spectroscopy of mass-selected molecular ions, Int. J. Mass Spectrom. 254 (2006) 1–19.
[69] R.E. Dickerson, H.R. Drew, B.N. Conner, R.M. Wing, A.V. Fratini, M.L. Kopka, The anatomy of A-, B-, and Z-DNA, Science 216 (1982) 475–485.
[70] S. Barbe, M. Le Bret, Effect of a water molecule on the sugar puckering of uridine, 2'-deoxyuridine, and 2′-O-methyl uridine inserted in duplexes, J. Phys. Chem. A 112 (2008) 989–999.
[71] L. Barnes, B. Schindler, A.-R. Allouche, D. Simon, S. Chambert, J. Oomens, I. Compagnon, Anharmonic simulations of the vibrational spectrum of sulfated compounds: Application to the glycosaminoglycan fragment glucosamine 6-sulfate, Phys. Chem. Chem. Phys. 17 (2015) 25705–25713.
[72] J. Oomens, J.M. Bakker, B.G. Sartakov, G. Meijer, G. von Helden, The infrared spectrum of the benzoyl cation, Chem. Phys. Lett. 367 (2003) 576–580.
[73] J. Oomens, A. Tielens, B.G. Sartakov, G. von Helden, G. Meijer, Laboratory infrared spectroscopy of cationic polycyclic aromatic hydrocarbon molecules, Astrophys. J. 591 (2003) 968–985.
[74] F. Calvo, Y. Li, D.M. Kiawi, J.M. Bakker, P. Parneix, E. Janssens, Nonlinear effects in infrared action spectroscopy of silicon and vanadium oxide clusters: Experiment and kinetic modeling, Phys. Chem. Chem. Phys. 17 (2015) 25956–25967.